ROSAT/ASCA OBSERVATIONS OF THE MIXED-MORPHOLOGY SUPERNOVA REMNANT W28

Jeonghee Rho

SIRTF Science Center, California Institute of Technology, MS 220-6, Pasadena, CA 91125,

e-mail:rho@ipac.caltech.edu

AND

Kazimierz J. Borkowski

Department of Physics, North Carolina State University, Raleigh, NC 27695

Received _____; accepted _____

ABSTRACT

We present three sets of ROSAT PSPC and four sets of ASCA observations of the supernova remnant (SNR) W28. The overall shape of X-ray emission in W28 is elliptical, dominated by a centrally-concentrated interior emission, sharply peaked at the center. There are also partial northeastern and southwestern shells, and both central and shell X-ray emission is highly patchy.

The ASCA spectra reveal emission lines of Ne, Mg, Si, and Fe Kα and continuum extending at least up to 7 keV, showing that X-ray emission in W28 is mostly of thermal origin with a hot thermal component. We found that spectral variations are present in W28. The southwestern shell can be fit well by a plane-shock model with a temperature of 1.5 keV and an ionization timescale of 1.5×10^{11} cm^{-3} s. The long ionization timescale combined with a low estimated electron density of ~ 0.2 cm^{-3} implies SNR age of several $\times 10^4$ yr. The low density in the southwest is consistent with the shock breakout away from molecular clouds in the north and northeast. The northeastern shell, with a lower temperature of 0.56 keV and a longer ionization timescale of 1.7×10^{13} cm^{-3} s, spatially coincides with the radiative shell delineated by radio and optical filaments. But a relatively high temperature and a low density of X-ray emitting gas in the northeastern shell indicate that we are not observing gas cooling from high temperatures. Unlike for the southwestern and northeastern shells, the central emission cannot be fit well by a single temperature model, but two components with temperatures of 0.6 keV and 1.8 keV are required. The long ionization timescales imply that the gas is close to the ionization equilibrium. The low temperature component is similar to those seen in other Mixed-morphology SNRs. The X-ray luminosity of W28 is $\sim 6 \times 10^{34}$ ergs s^{-1}, and the estimated X-ray mass is only $\sim 20 - 25 M_{\odot}$. A comparison of W28 with other typical Mixed-morphology SNRs reveals significant differences in its X-ray properties; W28 has a higher temperature and noticeable spectral variations.

W28 belongs to a class of SNRs considered by Chevalier (1999), with a radiative shell interacting with clumpy molecular clouds. X-ray emission at its center is a "fossil" radiation from gas which was shocked early in the evolution of the remnant, and its centrally-peaked morphology could have been caused by processes such as evaporation, electron thermal conduction, and mixing induced by various hydrodynamical instabilities. But W28 poses a challenge for existing models of X-ray emission, because the evaporation model of White & Long (1991) is in conflict with observations, while the presence of temperature variations seems

inconsistent with SNR models with efficient thermal conduction.

Subject headings: ISM: individual (W28) – supernova remnants – X-rays: ISM

1. Introduction

Supernova remnants (SNRs) can be classified into three broad categories based on their X-ray and radio morphologies. One class is those in which both the X-ray and radio morphologies are shell-like; most of shell-like SNRs have thermal X-rays, from a plasma heated by a shock wave (such as in Cas A). Some shell-like SNRs such as SN 1006 emit nonthermal synchrotron X-rays due to radiation from shock-accelerated electrons. The second class consists of the Crab-like remnants, also called plerions. The X-ray and radio morphologies of these are center-filled. Their energy source is an active pulsar (Seward 1985), and the X-ray spectrum is a featureless power law due to synchrotron processes. The third morphological category is a composite, simultaneously central emission and a shell (such as Vela and CTB 80). Recently we have classified a group of SNRs, which have centrally peaked X-ray and shell-like radio morphology, as a new, distinct morphological class which we term "mixed-morphology" (MM) supernova remnants (Rho & Petre 1998) or "thermal composite" SNRs (Jones et al. 1998). Members of this class include 3C391, W28, and W44. Despite their X-ray morphological similarity to the plerions all X-ray spectral evidence now clearly show that the X-ray emission is primarily thermal (Rho et al. 1994; Rho 1995; Rho & Petre 1998). ASCA observations revealed the presence of strong thermal line emission in many of these remnants: W44 (Harrus et al. 1997; Rho et al. 1994), Kes 27 (Rho et al. 1998), 3C391 (Chen & Slane 2001). The population of these mixed morphology SNRs is at least 10% of all known SNRs, and more than 25% among X-ray detected SNRs, suggesting that the mechanism for creating a remnant with the centrally-peaked thermal emission is not rare (Rho & Petre 1998).

The most important physical property of these remnants distinctly different from others is that their temperature profiles are uniform, rather than radially dependent. A radial temperature gradient is generally expected for a remnant of an SN explosion in a uniform ambient medium, such as in the classical Sedov solution. The uniform profile was first detected through spatially-resolved PSPC spectroscopy of W44 (Rho et al. 1994), and IC 443 (Asaoka & Aschenbach 1994; Rho et al. 1995). The spectral hardness maps of MSH 11-61A, CTB 1, W63, HB 3 (Rho 1995) and 3C400.2 (Saken et al. 1995) are smooth, also indicating uniform temperature profiles.

There are two competing scenarios which have been proposed to explain the centrally-filled morphology of mixed-morphology (MM) remnants: fossil radiation from the interior of a remnant in the shell-formation (radiative phase) stage (Cox et al. 1999; Chevalier 1999), and evaporation of interior clouds (White & Long 1991). The first hypothesis is *radiative model* in which the shell of an expanding SNR cools below $\sim 10^6$

K, and its X-ray emission becomes undetectable because of low temperatures and the ISM absorption. But X-rays from the hotter interior are still detectable as "fossil" thermal radiation (Seward 1985). Although dense environments of MM SNRs could hasten the onset of the shell-formation evolutionary stage, their uniform temperature profiles still stand in contrast to the radial temperature gradient expected from "fossil radiation." Recent work by Cox et al. (1999) and Shelton et al. (1999), however, suggests that thermal conduction significantly reduces the radial thermal gradient and thus it could explain the centrally-condensed X-ray morphology and the uniform temperature profiles observed in the MM SNRs.

The other hypothesis is the *evaporation model*, in which the enhanced interior X-ray emission could arise from gas evaporated from clouds. A model based on cloud evaporation (McKee 1982; White & Long 1991) reproduces some of properties of a number of MM remnants observed by Rho & Petre (1998). This model assumes SNR shock propagation through a cloudy ISM. Clouds which are too small to affect the blast wave propagation, but of sufficiently high density to survive passage through a strong shock, subsequently provide a reservoir of material inside the remnant cavity.

A correlation between molecular interacting SNRs and X-ray center-filled SNRs was suggested by Rho & Petre (1998). Recently Chevalier (1999) presented a framework for the SNR evolution in molecular clouds, where the radiative shell is interacting with clumpy molecular clouds. In his framework X-ray emission is a "fossil" radiation from the SNR interior, although he admits that the observed X-ray morphologies of MM SNRs might pose the greatest challenge for his models. Just like in the conduction models of Cox et al. (1999) and Shelton et al. (1999), thermal conduction might be crucial for explaining uniform temperature profiles in interiors of these remnants.

The supernova remnant W28 (G6.4-0.1) is an archetype MM SNR, showing center-filled X-rays and a shell-like radio morphology (Long et al. 1991). There are double radio shells in the northern part of the SNR, and the northeastern and eastern shells are apparent; the magnetic field lines are tangential over the northern shell (Frail, Kassim, & Weiler 1994; Shaver & Goss 1970; Kundu & Velusamy 1972). The radio spectral index is $\alpha \sim 0.4$ (Kassim 1992), where $S \propto \nu^{-\alpha}$. The *Einstein* IPC observation revealed that the X-ray emission is thermal with a temperature of 2.3×10^7 K (2 keV) and an intervening column density $N_H \sim 2 \times 10^{21}$ cm^{-2} (Long et al. 1991). Analysis of EXOSAT data also led to a high temperature of 2.5×10^7 K and a strong Fe Kα line at 6.7 keV was detected (Jones 1991). Torii et al. (1996) from their preliminary analysis of ASCA data reported that a combination of thermal and nonthermal models provided a good fit to X-ray spectra of W28.

Diffuse optical nebulosity was detected throughout most of the interior of W28 (van den Bergh 1978). W28 lies in a complicated region of the inner Galaxy which is confused by several large H II regions. Wootten (1981) suggested an interaction with a molecular cloud in W28, based on observations of broad CO (1-0) lines with FWHM of 11 km s^{-1} and the presence of warm dense clouds. A recent convincing detection of even broader lines (as large as 70 km s^{-1}) was reported by Arikawa et al. (1999) and Frail & Mitchell (1998) using CO (3-2) line. Arikawa et al. mapped shocked gas at the northern boundary, finding about 2000 $M_{\odot}$ of shocked molecular gas. Twenty-six shock-excited OH masers which are signposts of molecular interactions were also detected along the northern boundary and along the eastern shell of the remnant (Frail, Goss, & Slysh 1994; Claussen et al. 1999). In addition, the infrared H_2 S(3) and S(9) lines were seen with ISO (Reach & Rho 2000), together with strong atomic fine-structure infrared lines (such as C, N, O, Si, P and Fe), with the [O I] line ratios implying a high ($> 10^3$ cm^{-3}) medium density. All these observations provide an unambiguous evidence for interaction with molecular clouds in W28. The presence of molecular clouds visibly affects the overall shape of the remnant, which is far from uniform and circular, typical for SNRs; it is instead dented in the north and east where molecular clouds are located.

W28 has long been considered as a highly evolved remnant (e. g., see Lozinskaya 1992). In the north, gas behind the blast wave propagating through the interclump medium of molecular clouds collapsed into a radiative shell, which can be observed as filamentary emission at optical and radio wavelengths. Optical spectra typical of radiative shocks, the tangential orientation of the magnetic field (Milne & Dickel 1975), and an excellent correspondence between optical and radio emission (Dubner et al. 2000) provide irrefutable evidence that the northern half of W28 is in the late radiative stage of the SNR evolution. The weakness of the observed X-ray emission at the position of the northern radio shells adds further support for this conclusion. The blast wave most likely broke out of the molecular cloud in the south (Dubner et al. 2000).

Two candidates for a pulsar associated with W28 have been suggested (Andrews et al. 1983; Kaspi et al. 1993). A glitching pulsar PSR B1758-23 was detected at the northern boundary of W28 (Kaspi et al. 1993; Frail, Kassim, & Weiler 1994). This remnant might also be the gamma-ray source 2CG 006-00 (Ormes 1988; Esposito et al., 1996), and it might harbor a recently discovered soft gamma ray repeater, SGR 1801-23 (Cline et al. 2000).

The distance to W28 is uncertain, between 1.6–3 kpc (Clark & Caswell 1976; Milne 1979; Frail, Kassim, & Weiler 1994). The Σ-D relation and optical measurements suggest 1.8 kpc (Goudis 1976) and 2 kpc (Long et al. 1991), respectively. Based on the assumed association of PSR 1758-23 with W28 (Kaspi et al. 1993), a distance of 3 kpc was suggested using an H I absorption measurement toward this pulsar

(Frail, Kulkarni, & Vasisht 1993). However, this association was not confirmed by VLBA measurements of interstellar scattering toward the pulsar (Claussen et al. 1999). Recent CO observations of the shock interaction with the molecular cloud imply a distance of 1.8 kpc, adopting the rotation curve of Clemens (1985) for a galactocentric distance of the Sun of 8.5 kpc. Because the evidence for the interaction with molecular clouds is very convincing, we adopt 1.8 kpc as the distance to W28.

In this paper, we present ROSAT and ASCA images and spectral mapping of W28 using three sets of ROSAT and four sets of ASCA data, and we compare them to other MM SNRs. We interpret the results in the framework of an SNR evolution in molecular clouds. We also examine other nearby X-ray sources in the field of view and search for X-ray emission from the pulsar PSR B1758-23.

2. Observations

W28 was observed with the ROSAT Position Sensitive Proportional Counter (PSPC). The count rate is 5.78±0.11 cts s^{-1}, almost twice as much as the IPC count rate of 3.2 cts s^{-1} (Seward 1990). A total of three pointed observations were performed, with the observation parameters listed in Table 1. The total exposure time is 23,800 s. The 45′ remnant size extends beyond the central circular field of view of the PSPC, where the PSPC response is most uniform and sensitive. Therefore, an exposure correction was necessary in order to obtain the mosaiced image. We used the analysis techniques for extended objects developed by Snowden et al. (1994). The scattered solar X-rays, the time-dependent flux of short- and long-term enhancements, and background contamination were evaluated as three parameters of the total number of contaminating counts in each band, the gradient of the counts across the image, and the rotation angle of that gradient, and they were subtracted. Residual afterpulse events were also removed. The vignetting and detector-artifact corrected exposure maps, and modeled particle background maps (including the soft background using a background model) were created and applied to the data. After correction of three images for background and exposure time, the images were merged together, and smoothed using adaptive-filtering algorithm.

We used archival ASCA data in order to investigate spectral properties of W28 at moderate ($E/\Delta E = 60$ at 6 keV) spectral resolution. ASCA (Tanaka, Inoue, & Holt 1994) had two detector pairs: Gas Imaging Spectrometers (GIS2 and GIS3) and Solid-state Imaging Spectrometers (SIS0 and SIS1). The SIS covers an energy band of 0.5–10 keV and the GIS 0.6–10 keV. The on-axis angular resolution of the GIS and SIS is about 1–2 arcminutes. Four sets of ASCA data pointed toward the northeast, center (two

sets of data) and southwestern portion of the remnant were used, and the observational parameters are summarized in Table 1. We filtered the ASCA data using several criteria such as Cut off Rigidity (COR) and earth elevation (based on revision 2 processing).

We generated two ASCA mosaiced images in 0.6–10.0 keV and hard (3–10 keV) energy bands. We used 4 sets of GIS2 and GIS3 images with exposure correction and background subtraction (the GIS fields of view are marked in Figure 2). First, the instrument maps were generated using FTOOLS task "ASCAEFFMAP", and the effective exposure maps were generated by combining the instrument maps with exposure times ("ASCAEXPO"). To subtract the background, we used long-exposure blank sky observations from which all point-like sources brighter than 2×10^{-13} ergs s^{-1} cm^{-2} in the 2–10 keV range were removed. These files were generated using high latitude observations taken between June 1993 and December 1995 by the ASCA team (Ikebe et al. 1998). The outer detector edges beyond 17′ radius were removed. Then we mosaiced 4 sets of GIS images using "FMOSAIC".

3. Results

3.1. Images and Morphology

The mosaiced ROSAT PSPC image is shown in Figure 1. The coverage of the GIS ASCA observations is marked on the ROSAT PSPC image in Figure 2. The mosaiced ASCA image is shown in Figure 3, with the ROSAT contours superposed. The ASCA image is consistent with the ROSAT image, considering that its spatial resolution is much lower, only about 1′, and that it also includes photons with energies higher than 2 keV which could not be detected by ROSAT. The global shape is elliptical; X-ray emission is concentrated at the center and fills the entire interior of the remnant. The PSPC image reveals that the central emission is sharply peaked and highly patchy. Limb-brightened partial shell structures are present in the northeast and southwest, and the northeastern shell is also partially broken, with patchy structures. There are a few places showing highly structured X-ray emission: there are ear-like segments of limb-brightened northern shell and a sudden jump (northern flat boundary in Fig. 4) in surface brightness in the north. The X-ray surface brightness between the two ear-like patches (left patch is the northeastern shell and right patch is shown in Fig. 4) stays very flat from the east to west along Dec -23° 15′. The PSPC image is superposed on contours of a 328 MHz radio continuum image (Dubner et al. 2000) in Figure 5. The X-ray surface brightness is anticorrelated with radio morphology not only on large scales, but also on small scales: the eastern prominent radio shell is located outside the X-ray emission and the northern thin

inner radio shell is immediately outside the northern flat boundary of X-ray emission. In the north, double radio shells are present, which is probably due to projection, and in the southwest both X-ray and radio emission are faint but show a partial shell. The only places where the radio and X-ray emission match well are the two ear-like structures, reinforcing the suggestion that the emission here is from the shell. The northeastern shell matches well with the partial radio shell as shown in the radio superposed image. Faint emission is found in the southwest, apart from the main body of the remnant. This part of the SNR is seen faintly in X-ray and radio but not at optical wavelengths. This suggests that it is either a breakout region of the remnant, or that extinction is higher here. The X-ray emission may extend beyond the radio boundary in the west.

In the PSPC soft band ($E < 0.5$ keV) most of the emission arises from the central part of the remnant and a bright patch in the northeastern shell, as shown in Figure 6. We created a PSPC hardness map between energy band of 0.9–2.2 keV and 0.5–0.9 keV (i. e., bands 5–7 and bands 2–4 as defined by Snowden et al. 1991). We chose the energy boundary of 0.9 keV because the spectral peak of the PSPC spectrum appears at this energy (see Figure 10). A spectral hardness ratio (SHR) map, defined here as the ratio of the high energy band map to the low energy band map, can reveal absorption and/or temperature variations. A high value of SHR indicates a locally high column density or a high temperature. The hardness ratio map is superposed on the PSPC surface brightness contours in Figure 7. This hardness map shows that the emission is harder in the southwest and south than in the north and northeast. This is consistent with our spectral results that the southwestern shell has a higher temperature than that of northeastern shell, and possibly elsewhere in the remnant (see § 3.2). We generated an ASCA hard (3–10 keV) image as shown in Figure 8; the southwestern part is brighter in hard X-rays relative to the total energy ASCA map. The central bright peak is also bright at hard X-rays, and the hard energy maps give hint of hard emission at the patches of both ear structures and the northern boundary. A hard source appears in the lower right corner of the image in Figure 8, which position coincides with two IRAS sources and an A star (HD 313524).

In order to show clearly differences in the radio and X-ray morphologies, we compare X-ray and radio surface brightness profiles in Figure 9. We chose the strong X-ray peak ($\alpha = 17^h\ 57^m\ 23.2^s$, $\delta =$ -23°23′50.6″, B1950) as the center for this analysis. We divided the remnant into 5 sectors based on their different appearance in radio and X-ray images: NW, covering position angles between 285° - 360° (measured east of north); N, covering P.A. 0° to 45° and 250° to 360°; SW, 185° to 250°; SE, 85° to 160°; and northeast, 65° to 70°. All X-ray profiles peak at the center, while the radio profiles show a prominent shell in most directions, but weakest at the south and southwest. A noticeable feature of the X-ray surface

brightness is that it shows a shell structure in the northeast which coincides with the radio shell at 20′ distance from the center (see Figure 9).

The surface brightness is composed of 3 components: 1) innermost central part with centrally peaked brightness ($r_s < 2'$), 2) smooth component ($2' < r_s < 35'$), and 3) northeastern and southwestern shell (20–30′ in radius) components. In the innermost central region, the spectrum is rather hard, and this region can be seen in both hard and soft emission in Figure 8. The observed surface brightness distribution in the interior of W28 implies a radial density profile described by $n/n_c = 1 - r/R$, as shown in Fig. 9a, where $n(r)$ is plasma density as a function of distance r from the remnant's center, n_c is the central density, and R is the remnant's radius. This profile is steeper than profiles usually found in other mixed-morphology SNRs (Rho & Petre 1998). The overall shape of remnant is far from uniform and circular, typical for supernova remnants; it is dented in the north and east because of the presence of molecular clouds. Partial shell structures and X-ray features in the interior are often adjacent to molecular interaction sites, and appear particularly bright when projection effects allow for longer line-of-sight distances through the X-ray emitting gas. This most often happens in regions least affected by the irregular cloud geometry, such as the northeastern shell. The projection effects are not favorable in the north, where molecular clouds are located on the near (front) side of the remnant (Arikawa et al. 1999). Instead of a shell, we observe an abrupt drop in the X-ray surface brightness at the location of molecular clouds (the northern flat boundary).

3.2. Spectral Analysis using ASCA/ROSAT spectra

We extracted three sets of ASCA and ROSAT PSPC spectra for the northeastern shell, center and southwestern shell (see Figure 4). The GIS and SIS spectra were extracted from each of the three pointings (we used the long exposure of sequence 51022000 for central region). The central region spectra covered most of GIS and SIS fields of view in the central pointing (ad51022000; see Figure 2). The southwestern shell and the northeastern shell extraction regions follow the shapes of the shells as shown in Figure 4: for the southwestern shell, the extracted region is a $12' \times 8'$ ellipse inclined at PA 162°, and for the northeastern spectra, it is an $8\farcm2 \times 3\farcm2$ ellipse at PA 150°. The central spectra, after background subtraction, have count rates of 1.004±0.007 cts s^{-1} for GIS2, 0.734±0.006 cts s^{-1} for GIS3, 0.785±0.007 for SIS0, 0.950±0.008 cts s^{-1} for SIS1, and 0.704±0.015 cts s^{-1} for ROSAT PSPC. The southwestern shell spectra after background subtraction have count rates of 0.412±0.006 cts s^{-1} for GIS2, 0.320±0.006 cts s^{-1} for GIS3, 0.222±0.006 for SIS0, 0.174±0.005 cts s^{-1} for SIS1, and 0.765±0.015 cts s^{-1} for ROSAT PSPC. Constraints imposed by

the internal calibration source led to a reduction in the effective GIS3 extraction area, resulting in lower GIS3 count rates relative to GIS2. The northeastern shell spectra after background subtraction have count rates of 0.215±0.003 for SIS0, 0.276±0.005 cts s^{-1} for SIS1, and 0.357±0.007 cts s^{-1} for ROSAT PSPC. We did not use GIS spectra because the signal-to-noise ratio for this small region was too low to be useful.

The central spectra show emission lines of Ne, Mg, Si, and Fe Kα, and continuum at least up to 7 keV (Figure 10a). The presence of emission lines means that the emission is thermal despite the center-filled morphology, implying that X-rays are not powered by the pulsar like in the Crab Nebula. A single power law fit is significantly rejected. This spectrum is different from another archetype mixed-morphology SNR, W44, where no emission above 5–6 keV is reported. We examined the source-free background region to see if the Fe Kα line comes from the Galactic Ridge, but there is no evidence of Fe Kα in source-free background spectra. In addition, the Fe Kα line image confirms that the emission is from the remnant itself, primarily from the center and the southwestern shell.

When we compare the central spectra with the southwestern and northeastern shell spectra, we find noticeable differences. The southwestern spectrum (at RA 17^h56^m, Dec -23°35′, see Fig. 4) is much harder than the central spectrum as it can be seen in Figure 10a, while the northeastern shell spectrum (see Figure 10b) is softer than spectra in other regions of the remnant. In order to quantify these differences, we simultaneously fit the spectra to five sets of ROSAT/PSPC, ASCA/SIS0 and SIS1, and ASCA/GIS2 and GIS3 spectra. We used the collisional ionization equilibrium (CIE) thermal model (Mewe-Kaastra plasma model; Kaastra 1992), and nonequilibrium ionization (NEI) thermal models as implemented in XSPEC (Borkowski, Lyerly, & Reynolds 2001), which included updated Fe L-shell atomic data based on calculations by Liedahl, Osterheld, & Goldstein (1995). Fit parameters are tabulated in Table 2. The SW spectrum is fit well by the plane shock model with a high temperature of $kT_s = 1.2$ keV. A fit with a simpler single ionization timescale NEI model reproduced the spectra moderately well ($\Delta\chi^2 \sim 1.16$). The Sedov model for SW region yielded $kT_s = 1.2$ keV, and an ionization timescale of $n_e t = 3.6 \times 10^{11}$ cm^{-3} s. The northeastern shell is fit best by NEI model with a lower temperature of $kT_e = 0.56$ keV, and a longer ionization timescale of $n_e t = 1.7 \times 10^{13}$ cm^{-3} s, than those from the southwestern shell. The line-of-sight absorption toward the northeastern shell is $N_H = 0.8 \times 10^{22}$ cm^{-2}.

For the central spectra, one-temperature CIE or NEI models did not yield acceptable fits to the central spectra ($\Delta\chi^2 > 2.3$, and $\Delta\chi^2 > 1.8$, respectively). To reproduce the moderately strong Fe Kα line in the central region requires a second thermal component with a higher temperature (see Figure 10c). For the two-temperature model fitting, we used three steps in spectral fitting. First, we fit the Fe Kα line centroid

using a Gaussian model, arriving at $6.6^{+0.04}_{-0.10}$ keV, which allowed us to estimate ionization parameter. As the ionization timescale τ increases, Fe ions become more ionized, with electrons gradually removed from the L shell which results in a higher line emissivity and a line centroid shift to higher energies. For $\tau < 10^{10}$ cm^{-3} s, Fe ions are very underionized as compared to ionization equilibrium, and the Fe Kα line is produced mostly through fluorescence following K-shell ionization by electrons. The observed centroid implies an ionization time scale for the hot temperature component of $\sim 5 \times 10^{11}$ cm^{-3} s (e. g., see Fig. 2 of Borkowski & Szymkowiak 1997). As the second step, we constrained the temperature and Fe abundances using only hard energy band (4–10 keV) spectra, with the bremsstrahlung model for the continuum and a Gaussian line for Fe Kα. The constraint is 1.8 keV for the central region, and the Fe abundance is consistent with solar abundances. A single ionization timescale NEI model fit in the hard energy band alone also gave $\tau = 5 \times 10^{11}$ cm^{-3} s, 1.8 keV temperature, and approximately solar Fe abundance. The fits are summarized in Table 2. As the third step, we added a second, soft component (CEI model, single ionization timescale NEI model, or Sedov model), while the temperature and ionization timescale for the hot component were fixed to the values obtained in previous steps. A two-temperature NEI model reasonably well reproduced the observed spectra ($\Delta\chi^2 \sim 1.1$, see Figure 10d) with a hot temperature of $kT_{hot} = 1.8 \pm 0.5$ keV and ionization timescale of $\tau_h = 5 \times 10^{11}$ s cm^{-3}, and a low temperature of $kT_l = 0.6$ keV with $\tau_l = 2 \times 10^{12}$ s cm^{-3}. (We note that modeling with just 2 temperature components is merely a convenient way of quantifying temperature differences present in the remnant. Because multi-temperature plasmas might be expected in complex remnants such as W28, a considerable caution is required in interpreting results of the two-component fits.) Both NEI and Sedov models provide equally good fits for the soft component, with a high ionization parameter of $\sim 2 \times 10^{12}$ cm^{-3} s.

Torii et al. (1996) suggested the presence of nonthermal X-ray emission in the southwest. With the poor S/N SW spectra, the presence of nonthermal emission is still an open question, which cannot be completely ruled out at this time. But because we see Fe Kα line in GIS2 spectra of the SW region, we favor thermal over nonthermal origin for the high energy emission. If nonthermal component were present in SW spectra, we would have a combination of thermal and nonthermal emission, because thermal line emission from elements such as Mg and Si is certainly present at low energies. It is also possible that the hard X-ray continuum and the Fe Kα line come from different regions. We attempted to find differences in spatial distributions between the hard continuum and the Fe Kα line, but this attempt failed because of low count rates at high energies. Better data are needed to confirm that the southwestern emission is of purely thermal origin, and to study the remnant's morphology in the Fe Kα line and in the hard continuum.

The derived ISM absorption is higher in the SW than in the northeastern shell and the central part of remnant (see Table 2). Considering that the remnant is interacting with clouds in north, east, and northeast, one might expect an enhanced absorption in these regions of the remnant, just the opposite of what is observed. However, if there are clouds in front of the remnant in the SW, the line-of-sight absorption can still be high without any interaction between the remnant and clouds. This is the case of IC 443, where N_H is higher across the central part of remnant because of the presence of molecular clouds in the front of the remnant, although the interaction with the clouds is seen in the south (Rho, Petre, & Hester 1994). There is no optical emission detected in the SW part of W28 (van den Bergh 1978; Long et al. 1991; Winkler, in private communication) which seems to suggest that absorption is indeed higher in the SW. But an equally plausible explanation for the weakness of optical lines is simply the absence of radiative shocks in the breakout SW region of the remnant. More observations are needed in order to resolve this issue, because the poor S/N spectrum of the southwestern shell ultimately limits our ability to understand the origin of its relatively hard spectrum.

3.3. Other sources in the field of view including the pulsar

A glitching pulsar, PSR B1758-23, was detected at the northern boundary of W28 (Kaspi et al. 1993; Frail, Kassim, & Weiler 1994), at R.A. $18^h01^m19.859^s \pm 0.058^s$ and Dec. $-23°\ 06'17'' \pm 102''$. An association of this pulsar with W28 was suggested by Kaspi et al. (1993), with the pulsar distance estimated at 3 kpc (Frail, Kulkarni, & Vasisht 1993). We examined this region in detail and found that the PSPC surface brightness is 2.5 times higher than the background brightness. The pulsar position is marked on the PSPC image in Figure 11 (rp900395 set of data, 9.3 ks in duration). Within errors, the centroid coincides with the pulsar. The small number of detected counts was not sufficient to perform a spectral or a timing analysis. The X-ray PSPC count rate is $3.05(\pm 1.21)\times 10^{-3}$ counts s^{-1}, which implies a luminosity of 1.2×10^{32} ergs s^{-1}, assuming a line-of-sight absorption of 8×10^{21} cm^{-2} and a power law spectrum with $\Gamma = 2$ (equal to the spectral index of the Crab Nebula). The luminosity is less than 0.5% of the total X-ray luminosity of W28. A deeper observation is required to confirm whether this is true detection or not.

There are two X-ray sources to the east of the remnant. The northern source (R.A. $18^h02^m10^s$ and Dec. $-23°\ 33'38''$) is very soft, without a known counterpart. It is probably a stellar source, which we denote as RX1802-2333. The second (southern) source, located at R.A. $18^h01^m59.7^s$ and Dec. $-23°\ 41'20.8''$, is the HII region BFS 1, and its O-type star, CPD-23 6751, emits X-rays. There is another X-ray source in

the northeast which can be identified with another H II region, the Trifid nebula, whose observation (R.A. $18^h02^m23.35^s$ and Dec. $-23°\ 01'47.0''$) is reported elsewhere (Rho et al. 2001).

4. Discussion

Because W28 is a complex remnant in an advanced evolutionary stage, we first discuss its global kinematics and dynamics based on observations at wavelength bands other than X-rays. Next, we discuss and interpret X-ray observations. Finally we compare W28 with other mixed-morphology remnants.

4.1. Kinematics and Dynamics of W28

Fabry-Perot observations of the brightest optical emission at the center of W28 gave expansion velocity of 40 km s^{-1} (Lozinskaya 1974), with individual filaments moving with radial velocities up to 80 km s^{-1} and with the average Hα width of 40–50 km s^{-1}. This should also be the blast wave velocity if this optical emission projected near the center of W28 has the same origin as the radiative filaments seen at the northern edge of the remnant. Optical emission in the interior has a more diffuse, chaotic appearance than the filamentary emission usually associated with radiative shocks seen edge on. Such diffuse emission is generally seen in remnants at late stages of their evolution (Lozinskaya 1992), and might potentially be associated with other physical processes such as cloud evaporation (Long et al. 1991) or cooling of X-ray emitting gas in the remnant's interior. But at least some of this emission must be produced by the radiative blast wave seen in projection against the center of the remnant, in view of a generally good correlation between radio, optical, and molecular emission (Dubner et al. 2000). Kinematic information about the blast wave velocity obtained from Fabry-Perot observations is in a fair agreement with estimates of shocks speeds derived from optical spectroscopy: Bohigas et al. (1983) estimate shock velocities between 60 and 90 km s^{-1} from the ratio of [O III] λ5007 /Hα line strengths, while Long et al. (1991) derive velocities larger than 70 km s^{-1} from ratios of [N II] and [S II] line strengths to the Hα line strength. All available evidence based on optical observations suggests that the blast wave velocity v_s is $\leq$ 100 km s^{-1}, with considerable spatial scatter with velocities varying in the 60 – 100 km s^{-1} range.

Only upper limits on the preshock density n_0 ahead of the blast wave can be derived from optical and infrared observations. Long et al. (1991) obtained an upper limit for the electron density of 70 cm^{-3} from observations of the density sensitive [S II] λ6717/λ6731 line ratio. This is consistent with the density of

~ 100 cm^{-3} derived by Bohigas et al. (1983) from this line ratio. An upper limit of ~ 100 cm^{-3} from the [O III] $52\mu/88\mu$ line ratio (Reach & Rho 2000) is also consistent with this result. An average preshock density must be significantly lower than these upper limits, but by an uncertain factor which depends primarily on the magnitude of the magnetic field support. In addition, the observed optical emission may originate not only in the postshock cooling region. For example, there is some evidence for the presence of a faint H II region from variations in the optical line ratios across the remnant (Long et al. 1991). Neglecting contribution from a suspected H II region and in the absence of the magnetic field support, the inferred preshock density would be below 1 cm^{-3}.

Magnetic field is likely to be dynamically important in the shocked gas at temperatures where [S II] $\lambda6717/\lambda6731$ emission is produced. Magnetic pressure becomes equal to the gas pressure in the postshock cooling gas at densities $n_m = 240 v_s (n_0/10\mathrm{cm}^{-3})^{3/2} (B_0/10^{-5}\mathrm{G})^{-1}$ cm^{-3}, where B_0 is the preshock tangential field (Chevalier 1999). For shock velocity of 80 km s^{-1}, preshock density of 5 cm^{-3}, and $B_0 = 10^{-5}$ G, n_m is equal to 70 cm^{-3} which is just consistent with the upper limit derived from [S II] lines. The preshock density of 5 cm^{-3} is at the lower end of the typical density range of 5–25 cm^{-3} encountered in interclump media of galactic molecular clouds (Chevalier 1999), through which the blast wave propagates. This uncertain estimate depends strongly on the unknown value of B_0, and a possible contamination of the optical and infrared emission by an H II region means that the preshock interclump density might be higher than 5 cm^{-3}. A fiducial interclump density of 10 cm^{-3} (Chevalier 1999) might be consistent with observations.

The postshock cooling gas should be recombining into neutral hydrogen, which can be observed in emission and absorption in the 21 cm H I line. Based on the preshock density of 10 cm^{-3} and the remnant's size, it is possible to estimate the total mass of the neutral hydrogen in the swept radiative shell. The bright hemispherical northern part of W28, where most of the optical emission is located, is about 30′ in diameter (9.5 pc in radius at distance of 1.8 kpc), while the southern part is much fainter and about twice as large in the east-west direction. This suggests that the blast wave broke out of the molecular cloud in the south. For the bright northern part we estimate that about 700 $M_\odot$ should be present in the neutral shell. Radio observations in the 21 cm line suggest that there is neutral hydrogen associated with W28. From a rather sparse cross-pattern mapping, Koo & Heiles (1991) found an excess emission over the galactic background at the location of W28, some of it with radial velocities in excess of 100 km s^{-1} with respect to the systemic velocity of W28. Venger et al. (1982) reported a detection of an expanding H I envelope 82 pc in diameter, with mass of 6.9×10^4 $M_\odot$ and expansion velocity of 20 km s^{-1}, centered on W28. While they

identified this massive envelope with the expanding shell of W28, this interpretation is not consistent with information obtained at other wavelength bands. The emission and absorption in the 21 cm line in this region of the sky is apparently complex, and further studies of W28 and its neighborhood in the 21 cm line are warranted. Such studies could provide us with crucial information about the properties of the radiative shell.

A large amount of ionized gas is seen at optical wavelengths. Long et al. (1991) estimated the total Hα flux at 1.3×10^{-8} ergs cm^{-2} s^{-1}, which at 10^4 K temperature, ~ 70 cm^{-3} density, and 1.8 kpc distance implies the presence of 300 $M_\odot$ of ionized gas. This is comparable to the estimated mass of the radiative shell. For the preshock density of 10 cm^{-3}, blast wave velocity of ~ 100 km s^{-1} and radius R of 9.5 pc, we estimate that the ionizing radiation generated by the radiative blast wave falls short of producing the ionizing flux necessary to account for the observed Hα flux by at least one order of magnitude. An unknown additional source of ionizing radiation must be present within the remnant. Possible sources of ionizing radiation include evaporating clumps in the remnant's interior (Long et al. 1991) or gas cooling from X-ray emitting temperatures (e. g., Cox et al. 1999).

The remnant's age is approximately equal to $0.3R/v_s = 3.6 \times 10^4$ yr, with $R = 9.5$ pc and $v_s = 80$ km s^{-1}, and assuming that the remnant is in the snow-plow stage of the evolution. The estimated kinetic energy E of the explosion is 4×10^{50} ergs (using equation [26] of Chevalier 1974). This might be an underestimate because the blast wave most likely broke out of the molecular cloud in the south. We also note that the derived value of E depends strongly on the assumed distance d to the remnant ($E \propto d^{3.12}$, see § 1 for discussion on the uncertainty of the distance). From simple analytical estimates (e. g., see Blondin et al. 1998), the transition from the adiabatic (Sedov) stage to the radiative stage should have occurred at $t_{tr} \approx 8.6 \times 10^3 E_{51}^{4/17} n_1^{-9/17}$ yr, where E_{51} is the explosion energy in 10^{51} ergs, and preshock density n_1 is measured in units of 10 cm^{-3}. The radius and velocity of the shock at this time were equal to $7.4 E_{51}^{5/17} n_1^{-7/17}$ pc and $340 E_{51}^{1/17} n_1^{2/17}$ km s^{-1}. While cooling is important at t_{tr}, the cool radiative shell forms at about $1.5 t_{tr}$ (see Table 1 in Blondin et al. 1998), when the shock velocity dropped to $220 E_{51}^{1/17} n_1^{2/17}$ km s^{-1}.

Significant pressure variations must be present within the remnant. For $n_0 = 10$ cm^{-3} and $v_s = 80$ km s^{-1}, the average pressure p/k in the radiative shell is equal to 1.1×10^7 cm^{-3} K, while Frail & Mitchell (1998) obtain $p/k \sim 4.6 \times 10^7$ cm^{-3} K from observations of the Zeeman splitting in the OH 1720 MHz line. At two locations within W28, Claussen et al. (1999) detected an even stronger magnetic field, which would imply pressures $p/k \sim 4.6 \times 10^9$ cm^{-3} K. Such high pressures are expected to be generated by the impact

of the radiative shell with the molecular clumps (Chevalier 1999). Pressures should be lower than average in the southern and the southwestern parts of W28, but no pressure estimates are available in this faint breakout region from radio, optical, or infrared observations.

4.2. Interpretation of X-Ray Observations

The southwestern region has a shell-like morphology, with a fairly good correlation between the X-ray and radio emission, and optical emission from radiative shocks is not present. This suggests that perhaps description of the SW shell spectra in terms of plane-parallel shock and Sedov models might be appropriate. This is unlike the central region, where X-ray emission is of unknown origin and its center-filled morphology is different from the Sedov solution, while the northeastern shell is located in the radiative section of the remnant, close to dense molecular clouds with OH masers.

We use our spectral fits (Table 2) to estimate physical parameters for the SW region. The temperature is equal to 1.5 keV, implying a shock velocity of 1130 km s^{-1}. Electron density may be derived from emission measure in Table 2, equal to $3.5 \times 10^{56} d_{1.8}^2$ cm^{-3}, and from the estimated volume V of the X-ray emitting material. The size of the shell seen in this location is $8' \times 16'$, or 14×9 pc at 1.8 kpc distance. Assuming a comparable (14 pc) depth of the shell along the line of sight, we arrive at $V \sim 9 \times 10^{57} d_{1.8}^3$ cm^3. Then, $n_e = 0.22 f^{-1/2} d_{1.8kpc}^{-1/2}$ cm^{-3}, where f is a filling fraction of the X-ray emitting material within volume V. With the electron density of 0.22 cm^{-3} and ionization age of 1.5×10^{11} cm^{-3} s, the shock is about 2.2×10^4 yr old. This is consistent with the estimated remnant's age of 3.6×10^4 yr. The preshock hydrogen density n_0 is equal to 0.05 cm^{-3}, where $n_0 = n_e/4.8$ for cosmic abundance plasma and strong shock jump conditions. This density is 2 orders of magnitude lower than the interclump density in the northern radiative section of the remnant, consistent with the observed breakout morphology of W28. The thermal pressure p/k of the X-ray emitting plasma, equal to $\sim 5 \times 10^6$ cm^{-3} K, is as expected somewhat lower than pressures encountered in the bright northern hemisphere. One problem is the high shock speed of 1100 km s^{-1}, because with this speed the shock would propagate to a distance of 40 pc in 3.6×10^4 yr, which is much larger than the remnant's radius. In order to investigate this issue, we now discuss the SW shell in the framework of spherical (Sedov) shock models instead of plane shocks.

Our Sedov spectral model fit yielded $T_s = 1.2$ keV, and ionization timescale of 3.6×10^{11} cm^{-3} s. The shock temperature in Sedov model is defined as the temperature immediately behind the shock. These spectral parameters are consistent with the plane-parallel shock model fit parameters; for ion-electron

equipartition, we expect $T_{shock} = 1.27 T_{Sedov}$ (Borkowski, Lyerly, & Reynolds 2001). The ionization timescale τ_{Sedov} is defined as the product of the electron density immediately behind the shock and the remnant's age, but the mean ionization timescale of the gas is equal to 0.202 τ_{Sedov}, which should be equal to half of shock age, i.e., $\tau_{shock}/2$. Therefore, $\tau_{shock} \approx 0.404 \tau_{Sedov}$, which is consistent with results obtained from shock and Sedov spectral fits. The physical parameters of the remnant can be estimated from the Sedov spectral fit parameters. Using $T_s = 1.2$ keV and $n_e t = 3.6 \times 10^{11}$ cm^{-3} s in equations of Hamilton, Chevalier, & Sarazin (1983), we get shock velocity of 1000 km s^{-1}, age of 5100 yr, explosion energy of 2.2×10^{51} ergs s^{-1}, and preshock density of 0.5 cm^{-3}. The remnant's age estimated in this way is much lower than 3.6×10^4 yr, which is not surprising in view of the problem that the shock velocity is too high for the radius of W28, encountered with the plane shock analysis. There is an order of magnitude discrepancy between the preshock densities derived from the Sedov model and estimated from the emission measure. This discrepancy, coupled with the low estimated age, suggests that Sedov analysis probably does not apply to the breakout region of W28, for example, because of large density gradients expected there. It is then doubtful that the current shock velocity is as high as 1000 km s^{-1}. For example, material in the southwestern shell section could have been shocked long time ago, and then adiabatically expanded into the low density region on the periphery of the molecular cloud complex. In this case, the blast wave itself would have propagated in the low density medium ahead of the observed shell, and could be too faint to be detectable with ROSAT or ASCA. Observations with a higher spectral and spatial resolution, and with a higher S/N ratio are needed in order to resolve this issue. The absorbed flux (0.3-10 keV) from this shell section is $4.5(\pm0.4)\times10^{-12}$ ergs s^{-1} cm^{-2}, and unabsorbed flux is $4.0(\pm0.4)\times10^{-11}$ ergs s^{-1} cm^{-2}, which is equivalent to X-ray luminosity of L_x of $1.45\pm0.14 \times 10^{34}$ ergs s^{-1} at 1.8 kpc distance.

For central spectra, we estimated electron densities and filling factors using emission measures. The lower temperature component with 6.9×10^6 K (0.59 keV) has a density of $0.48 f_{cold}^{-1/2}$ cm^{-3} and the higher temperature component with 2.1×10^7 K (1.8 keV) has a density of $0.19 f_{hot}^{-1/2}$ cm^{-3}. Assuming that the hot and cold gases are in pressure equilibrium, and that the whole volume is filled with the emitting gas (i.e., $f_{cold} + f_{hot} = 1$), the filling factors of cold and hot gases are 0.4 and 0.6, respectively. Electron densities in low and high temperature components are 0.75 and 0.25 cm^{-3}. The thermal pressure p/k of 9.5×10^6 cm^{-3} K is of the same order as our estimates of the pressure in the radiative shell, but significantly less than in dense regions with OH masers. Using the best-fit two-temperature NEI model, we estimated the flux and luminosity of X-rays. The absorbed flux for the central region (using 2T vnei models) is $1.7\pm0.3\times10^{-11}$ ergs s^{-1} cm^{-2}, and unabsorbed flux is $8(\pm2)\times10^{-11}$ ergs s^{-1} cm^{-2}, which is equivalent to X-ray luminosity

of L_x of $2.9(\pm 0.7)\times 10^{34}$ ergs s^{-1}, which is twice as high as that of the SW region. The northeastern region spectral fit gives an X-ray luminosity similar to that of central region.

The limb brightened northeast region (the left "ear") has a shell-like appearance and it appears to be spatially coincident with radiative shell as indicated by a very good spatial match with bright radio and optical filaments (Dubner et al. 2000; see also Fig. 9). The temperature of the X-ray emitting gas is equal to 0.56 keV (6.5×10^6 K). This temperature is significantly higher than expected from a spherically symmetric remnant at the late radiative stage of the evolution with parameters as estimated above. For example, the postshock temperature at t_{tr} is equal to $0.14E_{51}^{1/17}n_1^{2/17}$ keV in the Sedov model. Falle (1981) demonstrated that the emission-measure weighted temperature of the X-ray emitting gas at times longer than t_{tr} is no longer related to the shock speed. It fluctuates instead by about 50% around the value just quoted until at least $10t_{tr}$ (see Fig. 8 in Falle 1981). This discrepancy between the expected and the observed temperature cannot be solved by simply postulating a much higher interclump density, because our density estimates based on the emission measure rule out very high densities of the X-ray emitting gas. Note however that it might be difficult to detect gas with very low temperatures because of the high ISM absorption along the line of sight to W28.

Our best estimate of the total X-ray emitting mass is $\sim 20 - 25d_{1.8}^{5/2}M_\odot$: most of it in the center and 8 $M_\odot$ in the northeastern and southwestern shells. This is less than expected from a radiative remnant with parameters appropriate for W28. Numerical calculations of Hellsten & Sommer-Larsen (1995) indicate that about 10% of the total shocked gas (by mass) is emitting in X-rays at 3.6×10^4 yr, for a model SNR remnant with $E_{51} = 1$ and $n_1 = 1$. We would then expect ~ 100 $M_\odot$ of X-ray emitting gas in W28, mostly at low (0.14 keV) temperatures. This is consistent with an analytical estimate of 120 $M_\odot$, using equation (33) of Cui & Cox (1992). The observed X-ray emission comes from a much smaller amount of hotter gas, suggesting a somewhat different SNR evolution than implied by standard spherically-symmetric SNR models in a uniform ambient medium. This is "fossil" radiation, a conclusion supported by long cooling timescales of the gas. We estimated cooling timescales using temperatures and densities derived above; for isobaric cooling this timescale is 6×10^6 yr in the SW, and 3.7×10^5 yr for northeastern shell gas. This is much longer than the age of the remnant, so that the X-ray emitting gas cannot be associated with fast radiative shocks or with gas cooling from high temperatures. Instead, this material was shocked much earlier in the evolution of the remnant, and its temperature and density may have been modified since then by processes such as evaporation, electron thermal conduction, and mixing induced by various hydrodynamical instabilities. We consider next whether the evaporation model of White & Long (1991) or

the conduction model of Cox et al. (1999) can explain the observed X-ray properties of W28.

The evaporation model of White & Long (1991) is in conflict with ASCA spectra. In this model, because of the short timescale of evaporative flows induced by saturated thermal conduction, heavy-element ions in gas evaporated from small clouds are strongly underionized with respect to CEI plasmas when they are mixed with the hot diffuse gas occupying most of the SNR interior. Other processes such as hydrodynamical instabilities would further hasten mixing with the hot gas, so that ionization should occur mostly in the hot diffuse gas. Long et al. (1991) obtained an age of only 2400 yr for W28 using the evaporation model, which in combination with electron densities estimated from emission measures implies the presence of strongly underionized gas in W28. But ASCA spectra reveal gas nearly in ionization equilibrium, with ionization timescales at least one or two orders of magnitude longer than expected. X-ray spectra alone are sufficient to reject evaporation model for W28. But perhaps a more convincing argument against this model is provided by the presence of radiative shocks in the northern half of the remnant, which are not expected in the nonradiative evaporative model considered by Long et al. (1991). The failure of this model for W28 further supports conclusions of Chevalier (1999) who argued against the White & Long (1991) model as the explanation for the MM SNRs.

The radiative shell model of Cox et al. (1999) and Shelton et al. (1999), in which electron thermal conduction modifies the interior of an SNR evolving in a uniform ambient medium, provides reasonable values for the central density and temperature. Using equations of (3) and (10) of Cox et al. (1999), with $E_{51} = 1$, $n_1 = 1$, and the Spitzer's conductivity coefficient, we arrive at the central electron density of 0.93 cm^{-3} at the present (3.6×10^4 yr) time. The central temperature of 0.52 keV is then obtained by equating the central pressure to the pressure within the radiative shell. There is obviously a good agreement with the densities and temperatures of the cool temperature component found in the central regions of W28. But the conduction model predicts an X-ray emitting mass which is even larger than in the standard radiative shell model without conduction considered by us previously, in apparent disagreement with observations. In addition, the surface brightness of W28 is too sharply peaked at the center in comparison with the conduction model (it is sharper than that of W44; see Rho & Petre 1998), and the clumpiness seen in X-ray images is in contrast to a smooth gas distribution expected in this model. But the most serious challenge for any models in which conduction plays a major role might be the presence of temperature gradients in W28. The observed temperature differences must have originated early in the remnant's evolution, before the radiative shell formed, when efficient conduction would have obliterated temperature gradients in the remnant's interior. Using a self-similar conduction model of Cui & Cox (1992), we find that at the time of

the shell formation at 1.3×10^4 yr, temperature dropped from its central value by a factor of 2 at a sphere enclosing the innermost 75 $M_\odot$ of X-ray emitting gas. In apparent conflict with the model predictions, we observe larger temperature differences within much smaller amounts of X-ray emitting gas. Efficient thermal conduction might be inconsistent with the observed X-ray properties of W28.

The X-ray properties of W28, in particular the simultaneous presence of hot (1.5 keV) and cold (0.5 keV) components with long ionization timescales, are in conflict with predictions of the evaporation model of White & Long (1991) and perhaps are inconsistent with predictions of the radiative shell model with conduction (Cox et al. 1999). Apparently evaporation is less important than postulated by White & Long (1991), and conduction might be less efficient than postulated in both models. The radiative shell interacting with clumpy molecular clouds, as considered by Chevalier (1999), seems to provide a suitable framework for W28. In this model, X-ray emission at the center is a "fossil" radiation, whose properties are not fully understood at this time. Uniform temperature gradients seen in MM SNRs led Chevalier (1999) to argue that conduction is generally important in their interiors. This argument cannot be used for W28 because of the presence of temperature variations, including a large-scale temperature gradient. This temperature gradient may be attributed to different preshock densities (and hence shock speeds) in the northeast and southwest, due to interaction with molecular clouds in the north and northeast, and the breakout in southwest. In absence of efficient conduction on spatial scales comparable to the radius of the remnant, appreciable temperature gradients of the opposite sign to density gradients are generally expected. Their presence in W28 suggests that conduction might have been at least partially inhibited by magnetic fields, perhaps preferentially in the direction perpendicular to the field lines of large-scale magnetic fields. Another possibility involves poorly understood mass and energy exchange processes between the hot and tenuous interclump medium and dense cool clumps of gas embedded in this medium. While idealized models dominated by either evaporation or by conduction failed to explain observations, conduction, evaporation and mixing induced by various hydrodynamical instabilities must still be present in view of the clumpy nature of molecular clouds. Their relative importance remains to be determined by comparing future model calculations with X-ray spectra and morphology of W28. W28 should provide a stringent test for future modeling because of the presence of the appreciable temperature variations.

4.3. Comparison of W28 and other mixed-morphology SNRs

Understanding of MM SNRs requires a careful assessment of their X-ray properties, so that competing models can be tested on the basis of their ability to explain these properties. For example, uniform temperature profiles characteristic of MM remnants are well explained by models with efficient thermal conduction, but the presence of large temperature gradients in even a small subset of these SNRs might pose a problem for these models. Because X-ray spectra revealed multitemperature plasma in W28, we contrast X-ray properties of W28 with other MM SNRs.

W28 is known to be an archetype MM SNR along with W44 (Long et al. 1991; Rho & Petre 1998), because both show typical mixed morphology with center-filled X-rays and the shell-like radio morphology. However, our images and spectral analysis show that X-ray properties of W28 are somewhat different. First, unlike in other known MM SNRs, a high temperature plasma is certainly present, as evidenced by the Fe Kα line and the thermal continuum extending up to 10 keV. The southwestern shell has a high temperature of 1.5 keV, and a high temperature component of 1.8 keV is also present at the center.

X-ray emitting gas in W44 has temperature of 0.4–0.9 keV without any hard emission above 6 keV present (Harrus et al. 1997; Rho et al. 1994). Other MM SNRs (e.g., see Rho & Petre 1998) such as MSH 11-61A (Rho 1995), HB21 (Lee et al. 2001), 3C391 (Rho & Petre 1996; Chen & Slane 2001), and 3C 400.2 (Saken et al. 1995; Yoshita et al. 2001), have gas in the temperature range of 0.4–0.9 keV. ASCA data of HB21 also imply a low temperature of 0.6 keV (Lee et al. 2001), similar to results based on ROSAT data (Rho & Petre 1998). Plasma temperatures in these MM SNRs are between 0.4–0.9 keV. Other remnants also have gas in this range of temperatures (Rho & Petre 1998). In contrast, there is gas with a much higher temperature of 1.5 keV in the southwestern shell and 1.8 keV in the central region of W28.

The second difference is the presence of spectral variations in W28, in contrast to other MM SNRs which have uniform temperatures as revealed by spectral mapping (Rho et al. 1994; Rho & Petre 1998). The spectrum of the southwestern region is different from the center. The southwestern spectrum seems to show a high (1.5 keV) temperature component alone without the soft component. This may be partially accounted for by a higher absorption along the line of sight in the SW, but the poor S/N spectrum of the SW region ultimately limits our ability to understand the origin of these spectral differences. The spectrum of the northeastern region is also different from the center. The northeastern spectrum seems to show a low (0.56 keV) temperature component alone without requiring a second component. The central spectrum is noticeably different from the southwestern and northeastern spectra. Our results show the presence of

pronounced spectral variations within W28, quite unlike what is seen in more typical MM SNRs. Another difference is that X-ray mass of W28 is much less than those of other MM SNRs such as W44 and 3C391 (Rho et al. 1994; Rho & Petre 1996).

W28 has still common characteristics with other MM SNRs; X-ray emission is thermal with rich line emission as shown by the ASCA spectra, and the spectral fitting implies that the abundances are close to solar (ISM) abundances, without any evidence for ejecta material. There is also the prominent central X-ray emission within the well-defined radio shell. Therefore, W28 is still an MM SNR, but with a number of different X-ray properties; 1) partial shells are present, 2) X-ray emission is extremely clumpy, particularly in the northeastern shell and at the center, 3) temperature is higher than in other MM SNRs, and 4) spectral variations are present due to temperature differences. The difference between the northeastern and southwestern shells appears to be related to differences in preshock densities, while both hot and cool components are present in the central region.

Recently discovered MM SNRs such as G359.1-0.5 (Bamba et al. 2000), Sgr A East (Maeda et al. 2001) and Kes 27 (Rho et al. 1998) also share some of these characteristics with W28. They show evidence for very hot temperatures (1.5 – 4 keV), and mixed morphology between X-rays and radio, and they are located in dense environments, possibly interacting with nearby clouds. Several of them even show evidence of SN ejecta, which strongly suggests that they are younger than more well-known MM SNRs W44 and 3C 391.

Summary

1. The overall shape of X-ray emission in W28 is elliptical, with the emission concentrated at the center of the remnant. The interior emission is sharply peaked at the center and its morphology is highly patchy. Partial shells are present in the northeast and southwest, and the northeastern shell also has a patchy, partially broken appearance. There are ear-like segments of limb-brightened shells in the northeast and northwest. The X-ray surface brightness between the two ear-like patches stays very flat from east to west along Dec -23° 15′. The surface brightness is composed of 3 components: 1) the innermost central region with centrally peaked brightness, 2) smooth component, and 3) northeastern and southwestern shell components. The observed surface brightness distribution in the SNR interior implies a radial density profile described by $n/n_c = 1 - r/R$, where $n(r)$ is plasma density as a function of distance r from the remnant's center, n_c is the central density, and R is the remnant's radius. This profile is steeper than profiles usually

found in other mixed-morphology SNRs. The overall shape of the remnant is far from uniform and circular, typical for supernova remnants; it is dented in the north and east because of the presence of molecular clouds.

2. The ASCA spectra show emission lines of Ne, Mg, Si, and Fe Kα, and continuum at least up to 7 keV. ASCA/ROSAT spectra reveal spectral variations across the remnant: while the southwestern and northeastern shells are fit well by a one-temperature model, the central emission requires a two-temperature model with hot and cold components. The southwestern shell can be fit well by the plane shock model with a temperature of 1.5 keV, an ionization timescale of 1.5×10^{11} cm^{-3} s, and a line-of-sight absorption of 1.2×10^{22} cm^{-2}. The northeastern shell has a lower temperature of 0.56 keV, a longer ionization timescale of 1.7×10^{13} cm^{-3} s, and $N_H = 0.8 \times 10^{22}$ cm^{-2}. Unlike for the southwestern and northeastern shells, the central emission cannot be fit well by a single temperature model. Two components are required, a hot temperature component with $kT_h = 1.8 \pm 0.5$ keV and a long ionization timescale of 5×10^{11} cm^{-3} s, and a low temperature component with $kT_l = 0.6$ keV, $n_e t = 2 \times 10^{12}$ cm^{-3} s. Note that with the possible exception of the SW shell, the long derived ionization timescales imply that the gas is close to the ionization equilibrium. The X-ray luminosity of W28 is 6×10^{34} ergs s^{-1} (this includes only regions observed by ASCA/SIS), and the estimated total X-ray mass is rather small, only $\sim 20 - 25 M_{\odot}$, much less than expected from standard SNR models.

3. Observations at wavelength bands other than X-rays strongly suggest that W28 is in a radiative stage of evolution, at least in the northern half of the remnant where the interaction with the molecular clouds has been detected. This remnant then belongs to a class of SNRs considered by Chevalier (1999), with a radiative shell interacting with clumpy molecular clouds, in which X-ray emission in the center is a "fossil" radiation. The properties of X-ray emitting gas are broadly consistent with this scenario, but when compared with standard spherically-symmetric SNR models in a uniform ambient medium, the gas is hotter, there is less X-ray emitting gas than expected, and of course the centrally-filled morphology cannot be explained by such models. The material which we are observing at the center was likely shocked early in the evolution of the remnant, and its temperature and density may have been modified since then by processes such as evaporation, electron thermal conduction, and mixing induced by various hydrodynamical instabilities. But the evaporation model of White & Long (1991) is in conflict with observations, and efficient thermal conduction might not be consistent with large temperature variations detected in W28. Both evaporation and thermal conduction might be less efficient than assumed in these idealized models, while the clumpy nature of molecular clouds plays an uncertain but perhaps even a crucial role in determining

X-ray morphology and spectra.

4. W28 differs from other known MM SNRs by: 1) the presence of hot (1.5 keV) gas, 2) spectral variations are clearly present, the SW shell is much hotter than the NE shell, and a mixture of hot and cold gas is present at the center, 3) X-ray emission is more knotty and clumpy than in other MM SNRs, and partial shell-like structures are present. The large scale temperature gradient seems to to be related to the ambient ISM density, with the cooler gas associated with the molecular clouds and the hotter gas with the fainter breakout region. The separation between X-ray emitting gas and radiative shocks emitting in infrared and optical is smaller than in other MM SNRs, more similar to shell-like SNRs.

5. We report a marginal excess of X-ray emission in the ROSAT image at the position of the pulsar, PSR B1758-23, which is located at the northern boundary of W28. The count rate implies a luminosity of 1.2×10^{32} ergs s^{-1}, assuming a line-of-sight absorption of 8×10^{21} cm^{-2} and a power law spectrum with $\Gamma = 2$ (equal to the spectral index of the Crab Nebula). In addition to the pulsar, two isolated X-ray sources appear a few arcminutes away from the eastern boundary. The northern source is a point source, likely a foreground star with no counterpart at other wavelengths. The southern source which appears to be extended, can be identified with an HII region.

We thank Robert Petre for helpful discussion about the earlier version of the paper, and Ho-Gyu Lee for help in generating ASCA mosaiced images. We also acknowledge very helpful comments and suggestions by an anonymous referee. This research has made use of data obtained from the High Energy Astrophysics Science Archive Research Center (HEASARC), provided by NASA's Goddard Space Flight Center. J. R. acknowledge the support of the Jet Propulsion Laboratory, California Institute of Technology, which is operated under contract with NASA.

Table 1: ROSAT and ASCA Observations of W28 (G6.4-0.1).

pointing	Sequence No.	observation date	exposure time (s)	center R.A.	center Dec.
ROSAT					
center	wp500129	Mar5, 92	4224	18:00:49	-23:22:33
NE	rp500236	Sep9-10, 93	10,476	18:01:12	-23:25:60
SW	rp500237	Sep 9, 93	9100	17:59:59	-23:31:60
ASCA					
NE	ad51014000	Mar4, 94	28,000	18:01:06.00	-23:13:51.6
center1	ad51022000	Mar4-Apr4, 94,	21,000	18:00:41.76	-23:26:36.6
SW	ad54003000	Mar31, 96	11,500	17:59:18.0	-23:45:56.5
center2	ad54003010	Mar31, 96	10,500	18:00:22.8	-23:20:18.0

Table 2: Spectral Fits and Inferred Physical Parameters

Region	Center			SW shell		NE shell
Model	A[a]	B[b]	C[c]	D[d]	E[e]	F[f]
$\Delta\chi^2$[g]	1.4	1.1	1.1	0.96	0.93	1.01
N_H (10^{22}cm^{-2})	$0.73^{+0.04}_{-0.06}$	0.66±0.06	0.79±0.15	1.28±0.25	$1.26^{+0.24}_{-0.16}$	0.77±0.08
Low temperature component						
kT_l (keV)	$0.58^{+0.04}_{-0.07}$	0.59±0.05	0.35±0.15	1.2 (>0.8)	1.5±0.2	0.56±0.06
τ_l (10^{12} cm^{-3} s)	–	2.0 (>1)	1.8 ($^{+2.7}_{-0.8}$)	$0.36^{+0.20}_{-0.16}$	$0.15^{+0.17}_{-0.09}$	17 (>7)
Abundance (fixed)		2/3		2/3		2/3
$EM_l/(4\pi d^2)$ (10^{12} cm^{-5})	4-5.3	3.5-4.6	6.3-8.5	0.8-1	0.9-1	1.9-2.3
High temperature component						
kT_h (keV) (fixed[h])		$1.8(^{+0.7}_{-0.5})$		–		–
τ_h (10^{12} cm^{-3}s) (fixed[h])		$0.5(^{+0.50}_{-0.43})$		–		–
Fe (fixed)		$1.1(^{+0.9}_{-0.6})$		–		–
$EM_h/(4\pi d^2)$ (10^{12} cm^{-5})		0.65-0.8		–		–
Angular Diameter			$50'\times45'$			
Shell Radius		–		$28'$ ($14.5\times d_{1.8kpc}$ pc)[i]		$18'$ ($9.5\times d_{1.8kpc}$ pc)[j]
n_e (cm^{-3}, from EM)	$0.48(d_{1.8kpc}f)^{-1/2}$, $0.19(d_{1.8kpc}f)^{-1/2}$			$0.22(d_{1.8kpc}f)^{-1/2}$		$0.65(d_{1.8kpc}f)^{-1/2}$
Flux (ergs s^{-1} cm^{-2})		8×10^{-11}		4×10^{-11}		4.5×10^{-11}
Luminosity (ergs s^{-1})		$2.9\times10^{34}d^2_{1.8kpc}$		$1.45\times10^{34}d^2_{1.8kpc}$		$1.63\times10^{34}d^2_{1.8kpc}$

[a] *mekal + nei*

[b] *nei + nei*

[c] *sedov + nei*

[d] *sedov*

[e] *pshock*

[f] *nei*

[g] $\Delta\chi^2$ is reduced χ^2, and typical degree of freedom is ~650. The errors of the best fits for each region with 99% confidence are given.

[h] kT_h and the Fe abundance were determined from fits to the high energy (4-10 keV) spectra alone, and τ_h is determined using the Fe Kα line centroid.

REFERENCES

Andrews, M. D., Basart, J. P., Lamb, R. C., & Becker, R. H. 1983, ApJ, 266, 684

Arikawa, Y., Tatematsu, K., Sekimoto, Y., & Takahashi, T. 1999, PASJ, 51, L7

Asaoka, I., & Aschenbach, B. 1994, A&A, 284, 573

Bamba, A., Yokogawa, J., Sakano, M., & Koyama, K. 2000, PASJ, 52, 259

Blondin, J. M., Wright, E. B., Borkowski, K. J., & Reynolds, S. P. 1998, ApJ, 500, 342

Borkowski, K., Lyerly, W. J., & Reynolds, S. P. 2001, ApJ, 548, 820

Borkowski, K. J., & Szymkowiak, A. E. 1997, ApJ, 477, L49

Bohigas, J., Ruiz, M. T., Carrasco, L., Salas, L., & Herrera, M. A. 1983, RMxAA, 8, 155

Chen, Y., & Slane, P. O. 2001, ApJ, 563, 202

Chevalier, R. A. 1974, ApJ, 188, 501

Chevalier, R. A. 1999, ApJ, 511, 798

Clark, D. H., & Caswell, J. L. 1976, MNRAS, 174, 267

Claussen, M. J., Goss, W. M., Frail, D. A., & Desai, K. 1999, ApJ, 522, 349

Clemens, D. P. 1985, ApJ, 295, 422

Cline, T., et al. 2000, ApJ, 531, 407

Cox, D. P., et al. 1999, ApJ, 524, 179

Cui, W., & Cox, D. P. 1992, ApJ, 401, 206

Dubner, G. M., Velázquez, Goss, W. M., & Holdaway, M. A. 2000, AJ, 120, 1933

Esposito, J.A., Hunter, S.D., Kanbach, G., & Sreekumar, P., 1996, ApJ, 461, 820

Falle, S. A. E. G. 1981, MNRAS, 195, 1011

Frail, D. A., Goss, W. M., & Slysh, V. I. 1994, ApJ, 424, L111

Frail, D. A., Kassim, N. E., & Weiler, K. W. 1994, AJ, 107, 111

Frail, D. A., Kulkarni, S. R., & Vasisht, G. 1993, Nature, 365, 136

Frail, D. A., & Mitchell, G. F. 1998, ApJ, 508, 690

Goudis, C. 1976, Ap&SS, 45, 133

Hamilton, A. E. S., Chevalier, R. A., & Sarazin, C. L. 1983, ApJS, 51, 115

Harrus, I. M, Hughes, J. P., Singh, K. P., Koyama, K., & Asaoka, I. 1997, ApJ, 488, 781

Hellsten, U., & Sommer-Larsen, J. 1995, ApJ, 453, 264

Ikebe, Y., et al. 1998, ASCA Newsletter No. 3

Jones, L. R. 1991, in Iron Line Diagnostics in X-ray Sources, eds. A.Treves, G.C.Perola, & L.Stella, (Springer-Verlag: Berlin: Heidelberg: New York), 45

Jones, T. W., et al., 1998, PASP, 110, 125

Kaastra, J. S. 1992, An X-ray Spectral Code for Optically Thin Plasmas (SRON-Leiden Report)

Kaspi, V. M., Lyne, A. G., Manchester, R. N., Johnston, S., D'Amico, N., & Shemar, S. L. 1993, ApJ, 409, L57

Kassim, N. E. 1992, AJ, 103, 943

Koo, B.-C., & Heiles, C. 1991, ApJ, 382, 204

Kundu, M. R., & Velusamy, T. 1972, A&A, 20, 237

Liedahl, D. A., Osterheld, A. L., & Goldstein, W. H. 1995, ApJ, 438, L115

Lee, H.-G., Rho, J., Koo, B.-C., Petre, R., & Decourchelle, A., 2001, BAAS, 198, 4002L

Long, K., Blair, W. P., Matsui, Y., & White, R. L. 1991, ApJ, 373, 567

Lozinskaya, T. A. 1974, SvA, 17, 603

Lozinskaya, T. A. 1992, Supernovae and Stellar Wind in the Interstellar Medium, (American Institute of Physics: New York)

Maeda, Y., et al., 2001, ApJ, in press (astro-ph/0102183)

McKee, C. F. 1982, in Supernovae: A Survey of Current Research, (Reidel: Dordrecht), 433

Milne, D. K. 1979, Austr. J. Phys., 32, 83

Milne, D. K. & Dickel., J. R. 1975, Austr. J. Phys., 28, 209

Ormes, J. F., Ozel, M. E., & Morris, D.J. 1988, ApJ, 334, 722

Rho, J.-H., 1995, Ph.D. thesis, University of Maryland

Rho, J., Corcoran, M. F., Chu, Y.-H., & Reach, W. T. 2001, ApJ, in press

Rho, J., & Petre, R. 1996, ApJ, 467, 698

Rho, J., & Petre, R. 1998, ApJ, 503, L167

Rho, J., Petre, R., & Hester, J. J., 1994, The soft X-ray Cosmos, eds. E.M.Schlegel & R.Petre, (American Institute of Physics: New York), 318

Rho, J.-H., Petre, R., Schlegel, E. M., & Hester, J. J. 1994, ApJ, 430, 757

Rho, J., et al. 1998, BAAS, 193, 740

Reach, W. T., & Rho, J. 1999, ApJ, 511, 836

Reach, W. T., & Rho, J. 2000, ApJ, 544, 843

Shaver, P. A. & Goss, W. M. 1970, Aust. J. Phy. Astr. Sup., 14, 77

Saken, J. M., Long, K. S., Blair, W. P., & Winkler, P. F. 1995, ApJ, 443, 231

Seward, F. D. 1985, Comm. Astroph. XI, 1, 15

Seward, F. D. 1990, ApJS, 73, 781

Shelton, R., et al. 1999, ApJ, 524, 192

Snowden, S. L., McCammon, D., Burrows, D. N., & Mendenhall, J.A. 1994, ApJ, 424, 714

Tanaka, Y., Inoue, H., & Holt, S. S. 1994, PASJ, 46, L37

Torii, K., Tsunemi, H., Kaneda, H., & Slane, P. 1993, in UV and X-ray spectroscopy of Astrophysical and Laboratory Plasmas, eds. K. Yamashita & T. Watanabe, (Universal Academy Press: Tokyo), 291

van den Bergh, S. 1978, ApJS, 38, 119

Venger, A. P., et al., 1982, SvA, 26, 12

White, R. L., & Long, K. S. 1991, ApJ, 373, 543

Wootten, A. 1981, ApJ, 245, 105

Yoshita, K., Tsunemi, H., Miyata, E., & Mori, K. 2001, PASJ, 53, 93

This manuscript was prepared with the AAS LaTeX macros v4.0.

Fig. 1.— The mosaiced ROSAT PSPC image (0.5-2.4 keV) of W28. The grey-scale ranges from 0.0008 to 0.029 counts s^{-1} $arcmin^{-2}$.

Fig. 2.— ASCA GIS fields of view (four pointings) superposed on the ROSAT image.

Fig. 3.— ASCA greyscale image (0.5-10 keV) and PSPC contours. The grey-scale image range is (1.0 - 5.5) $\times 10^{-5}$ counts s^{-1} $arcmin^{-2}$.

Fig. 4.— Spectral extraction regions (solid circle and ellipses) superposed on the PSPC image. Right "ear-like" structure and northern flat boundary are also marked (dashed lines).

Fig. 5.— The PSPC greyscale image superposed on contours of the 328 MHz radio continuum image (from Dubner et al. 2000): the radio morphology is shell-like and X-rays are centrally peaked.

Fig. 6.— Soft ($E < 0.5$ keV) PSPC X-ray image superposed on PSPC total brightness contours. The greyscale is from 0.0008 to 0.0043 counts s^{-1} $arcmin^{-2}$.

Fig. 7.— The PSPC spectral hardness ratio (0.9–2.2 keV/0.3–0.9 keV) image with a greyscale range from 1.1 to 1.4, superposed on PSPC total brightness contours. The southern half of the remnant is harder than the northern half.

Fig. 8.— Hard (3–10 keV) ASCA image superposed on PSPC contours. The southwestern shell and center are harder than the northeast. The grey-scale image range is (1 - 3) $\times 10^{-5}$ counts s^{-1} $arcmin^{-2}$.

Fig. 9.— X-ray (*solid line*) and radio (*dotted line*) surface brightness profiles of W28 in the north (a), southwest (b), southeast (c), and northeast (d). Position angles are marked in each panel. The X-ray surface brightness is centrally peaked, but there are also shell structures at about 20′ from the center in the southwest and northeast. The dashed line in the northern sector corresponds to a radial density profile described in the text.

Fig. 10.— Comparison of W28 spectra for various regions. The best fits are shown, which are derived using 5 spectra from SIS0, SIS1, GIS2, GIS2 and ROSAT PSPC. (a) The central (*crosses*) and SW (*squares*) SIS0 spectra. Soft component is not present in the SW. (b) ASCA SIS spectra of the northeastern shell. The best-fit NEI model with $kT_e = 0.56$ keV, $N_H = 0.8 \times 10^{22}$ cm^{-2}, and the residuals are shown. (c) The ASCA SIS and ROSAT/PSPC spectra of W28 for the central region showing hard emission and the Fe Kα line. A two-temperature NEI model with $kT_h = 1.8 \pm 0.5$ keV and $kT_l = 0.6$ keV is also shown. (d) Two-temperature model of the central spectrum (only SIS0 spectrum is shown) with the hot and cold components indicated (total – *solid line*, cold – *dash-dotted*, hot – *dotted*).

Fig. 11.— A portion of the PSPC image with the pulsar position marked. Its position is at least 30″ away from a weak X-ray peak. The ellipse is an error box of the pulsar position. The diffuse emission is northern part of W28.

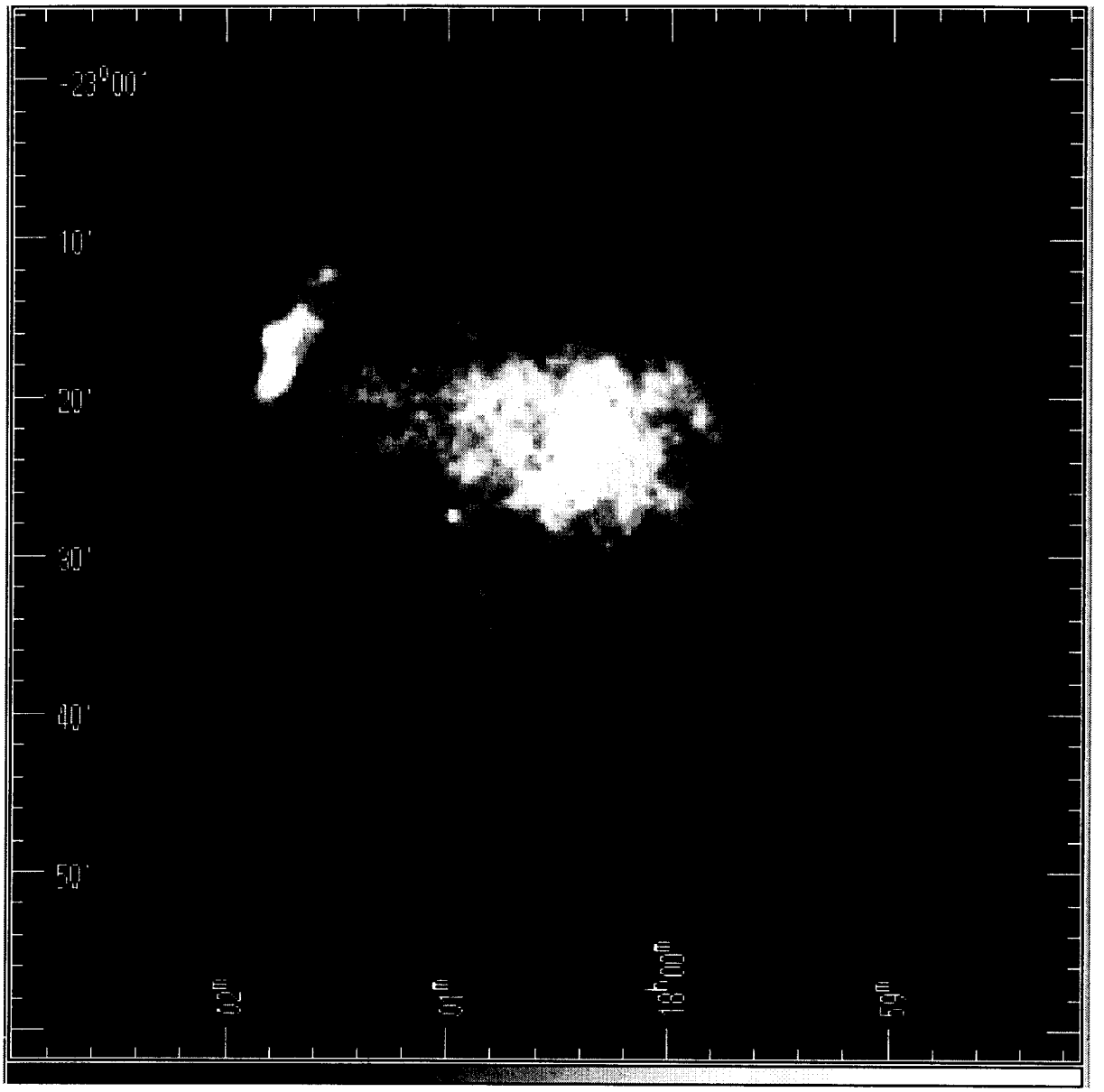
-23°00'
10'
20'
30'
40'
50'
18h00m

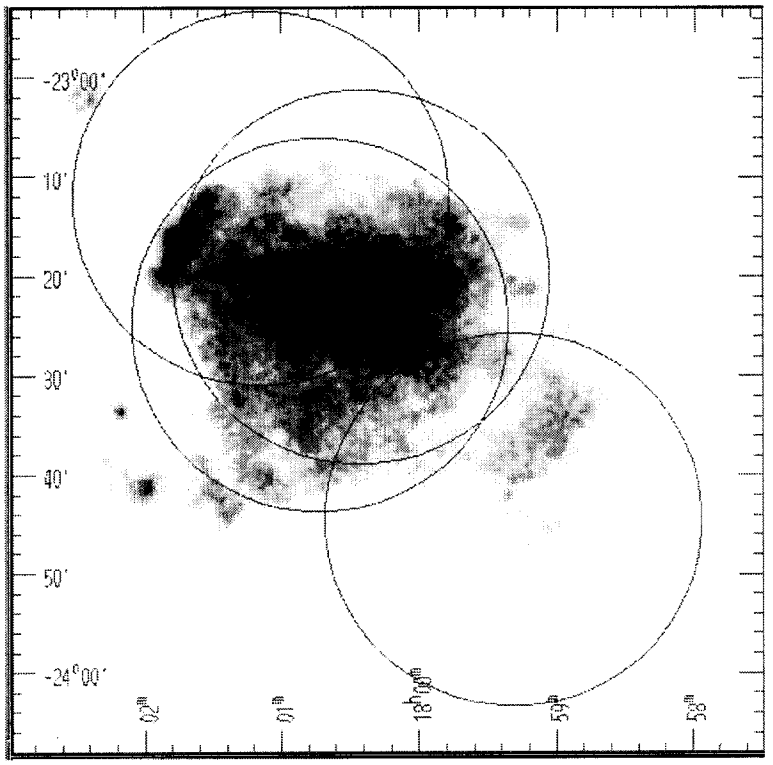

Fig. 2

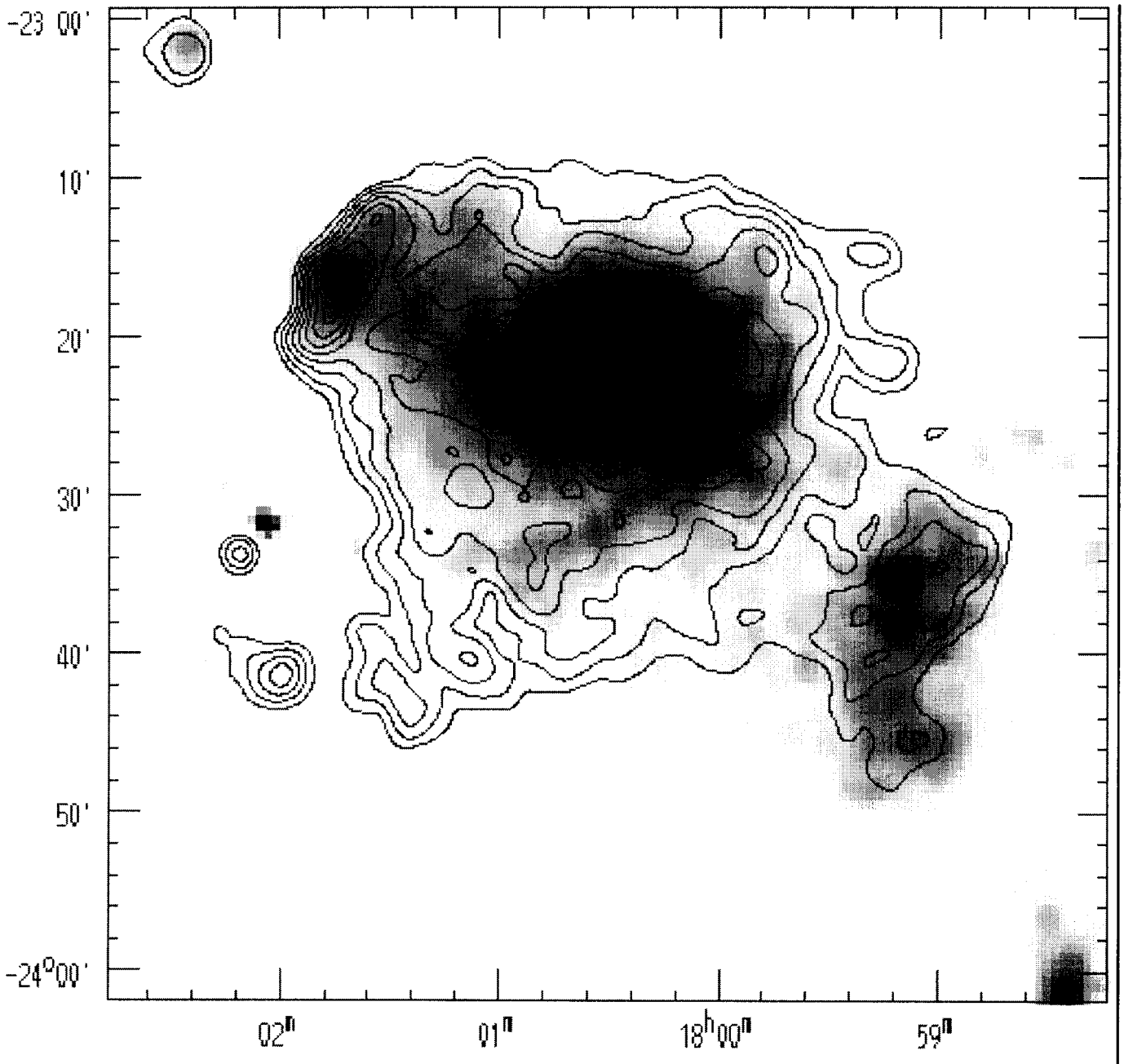

Fig. 3

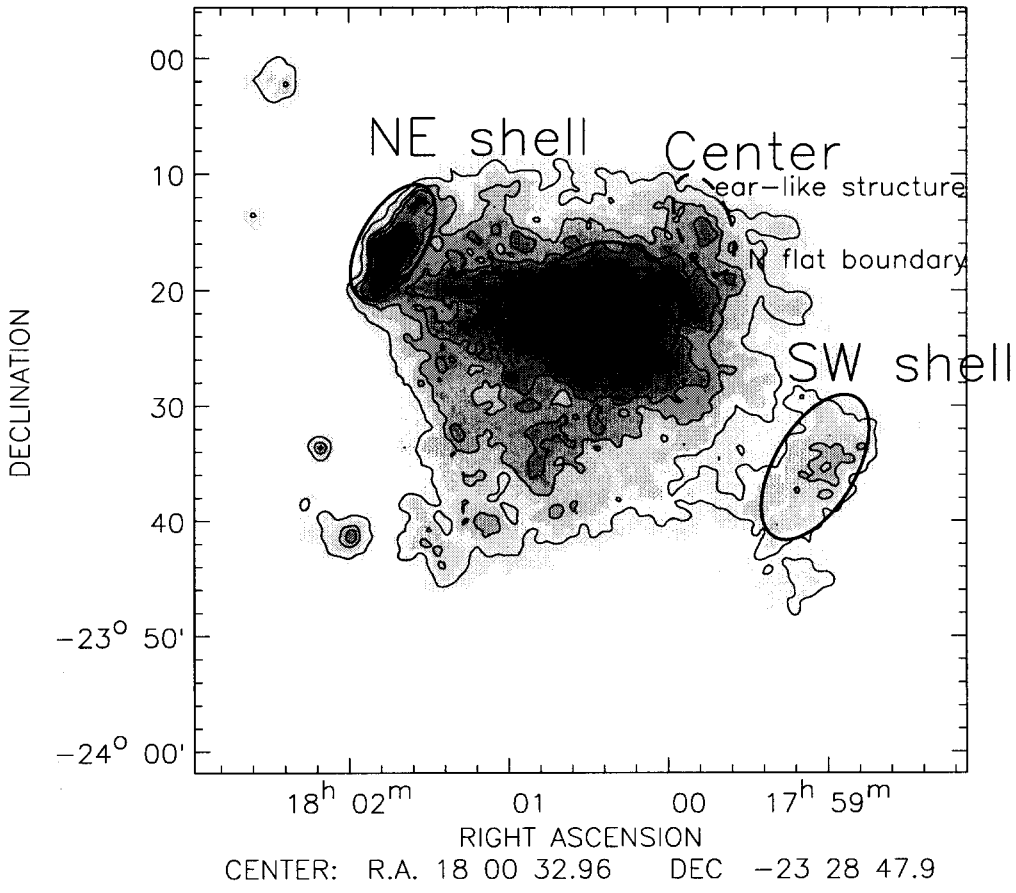
NE shell
Center
ear–like structure
N flat boundary
SW shell
DECLINATION
00
10
20
30
40
−23° 50'
−24° 00'
18h 02m
01
00
17h 59m
RIGHT ASCENSION
CENTER: R.A. 18 00 32.96 DEC −23 28 47.9

Fig. 4

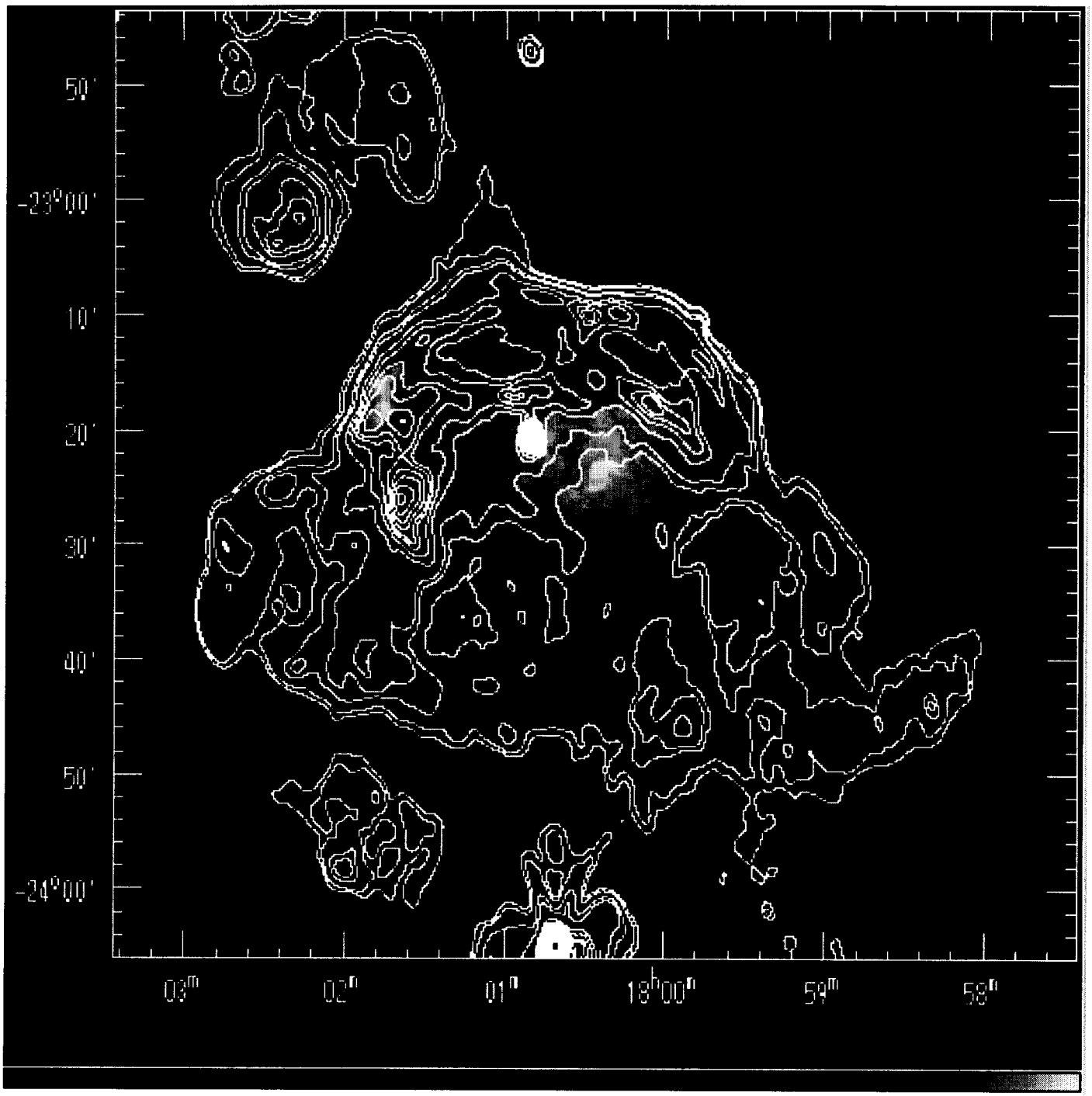

Fig. 5

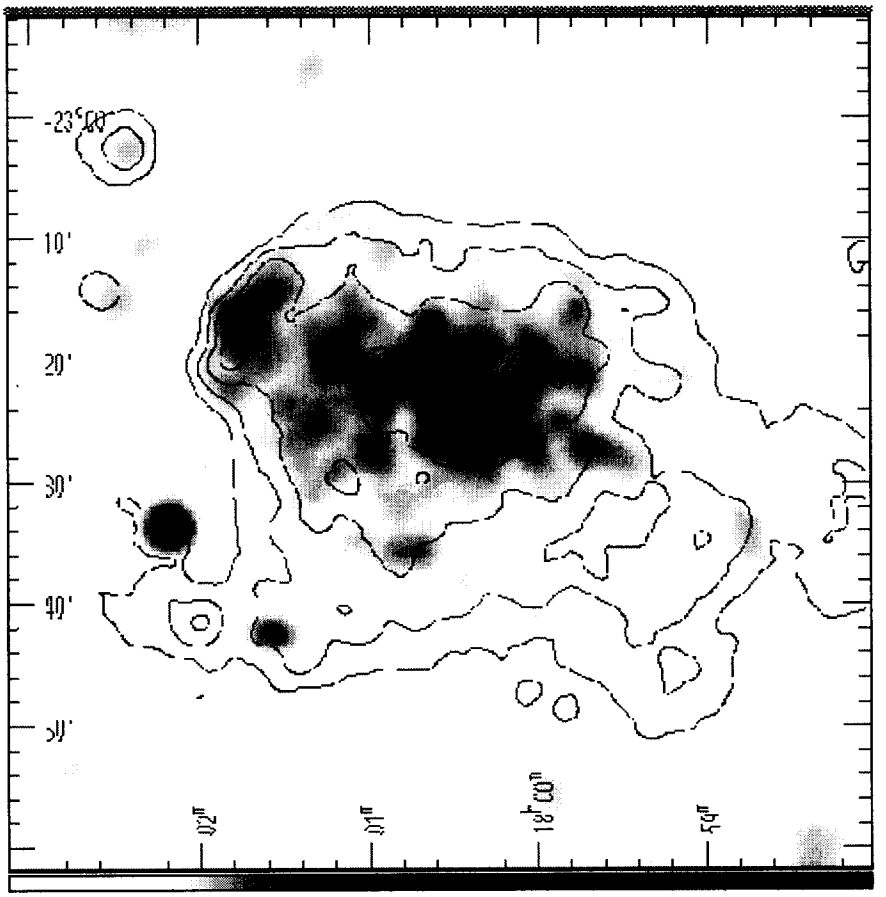
-23°00'
10'
20'
30'
40'
50'
02"
01"
18h00m
59"

Fig. 6

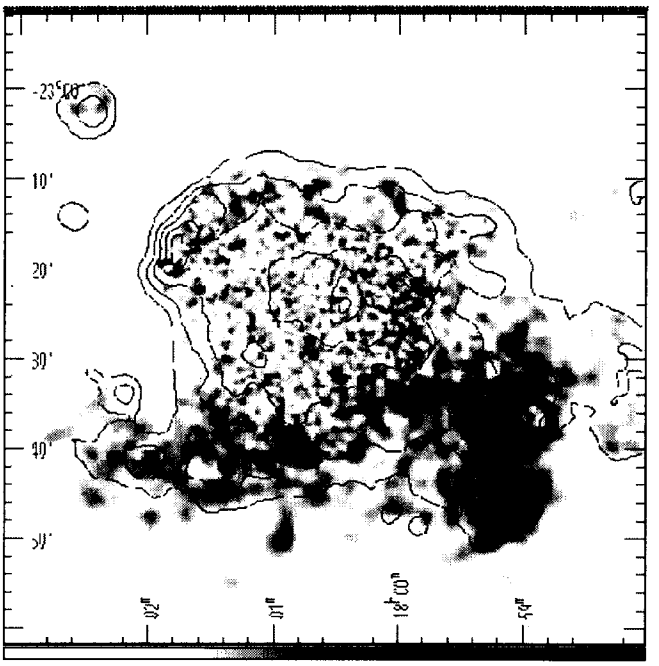

Fig. 7

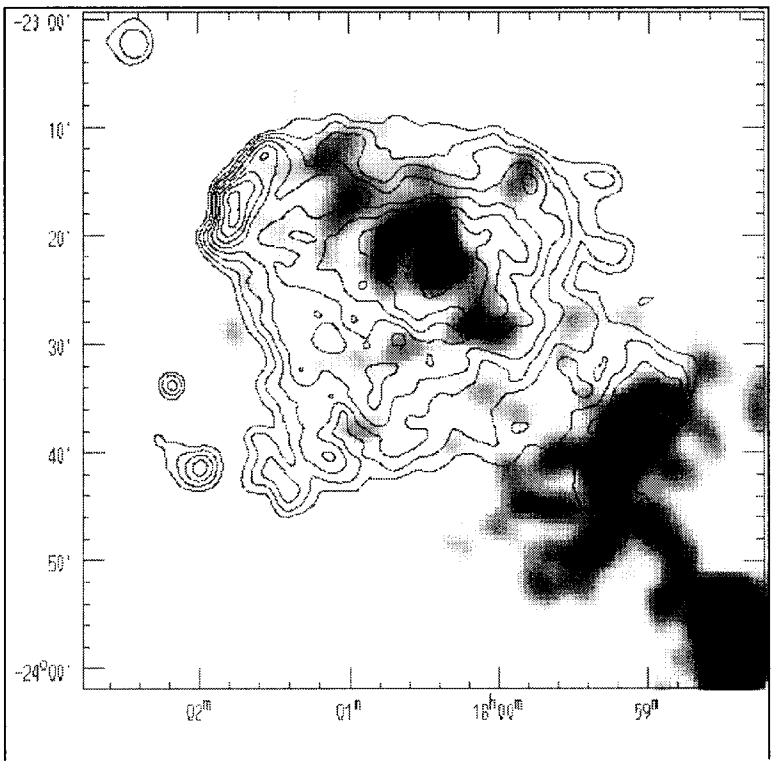

Fig. 8

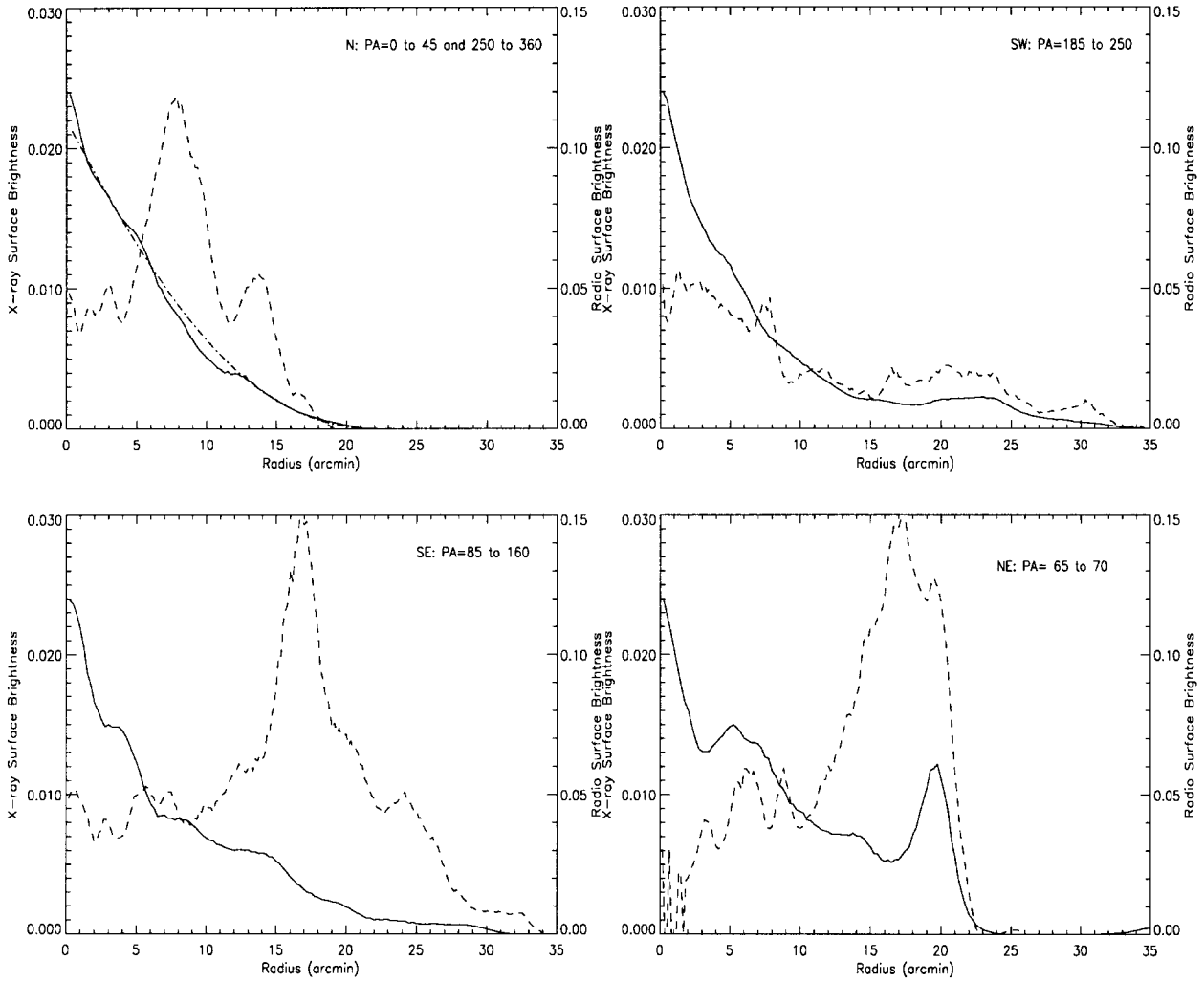
N: PA=0 to 45 and 250 to 360
SW: PA=185 to 250
SE: PA=85 to 160
NE: PA= 65 to 70
X-ray Surface Brightness
Radio Surface Brightness
Radius (arcmin)
0.030
0.020
0.010
0.000
0.15
0.10
0.05
0.00
0
5
10
15
20
25
30
35

Fig. 9

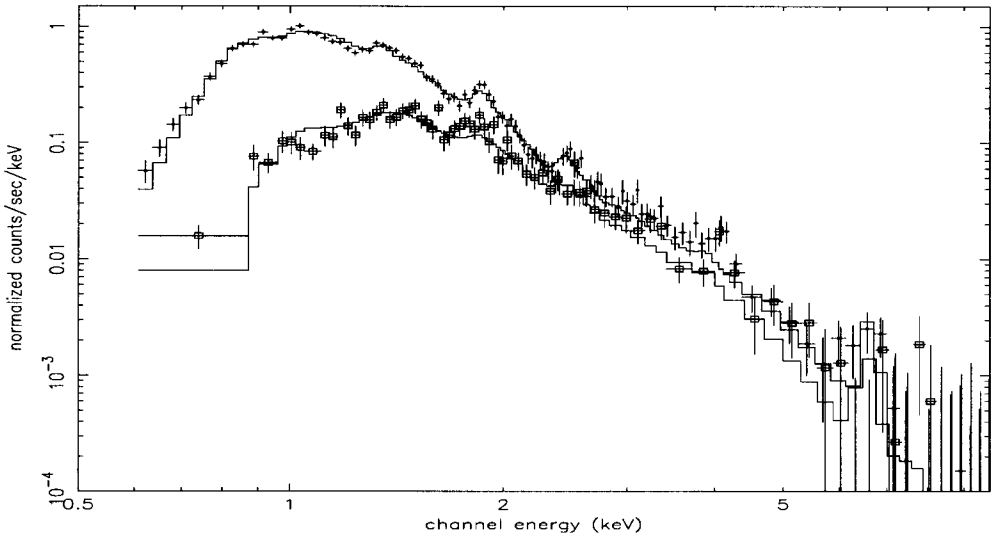

Fig. 10a

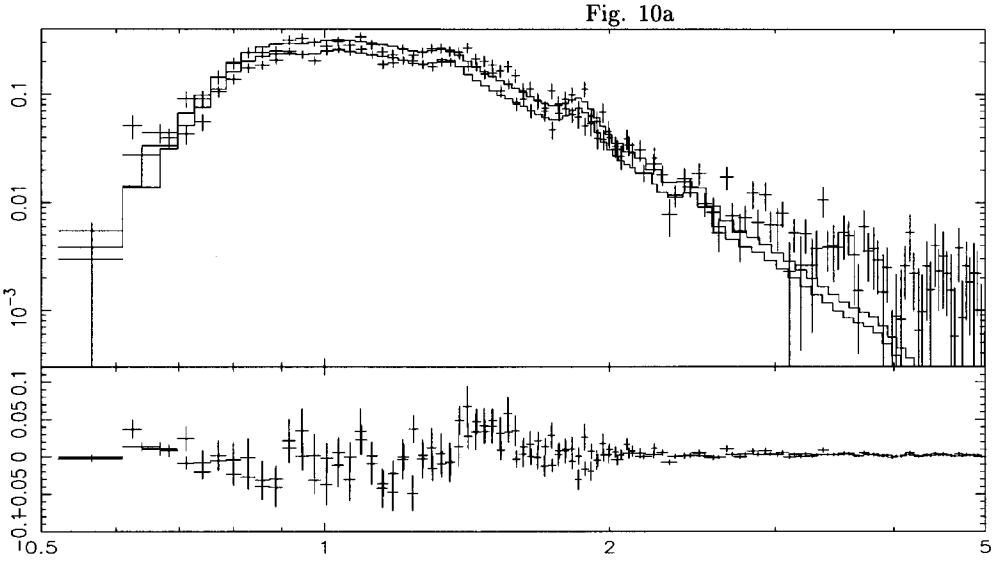

Fig. 10b

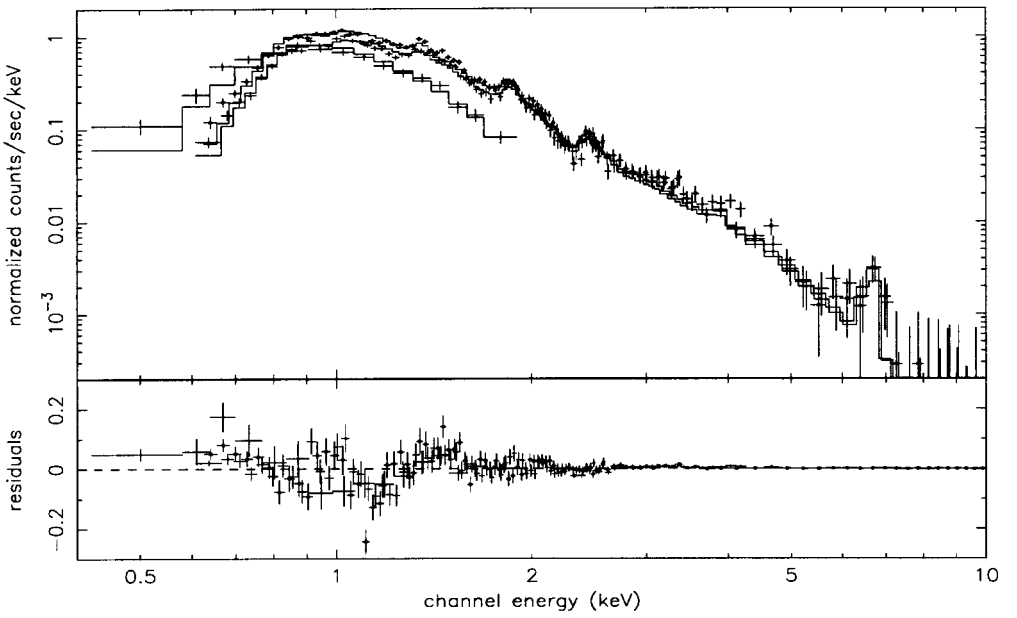

Fig. 10c

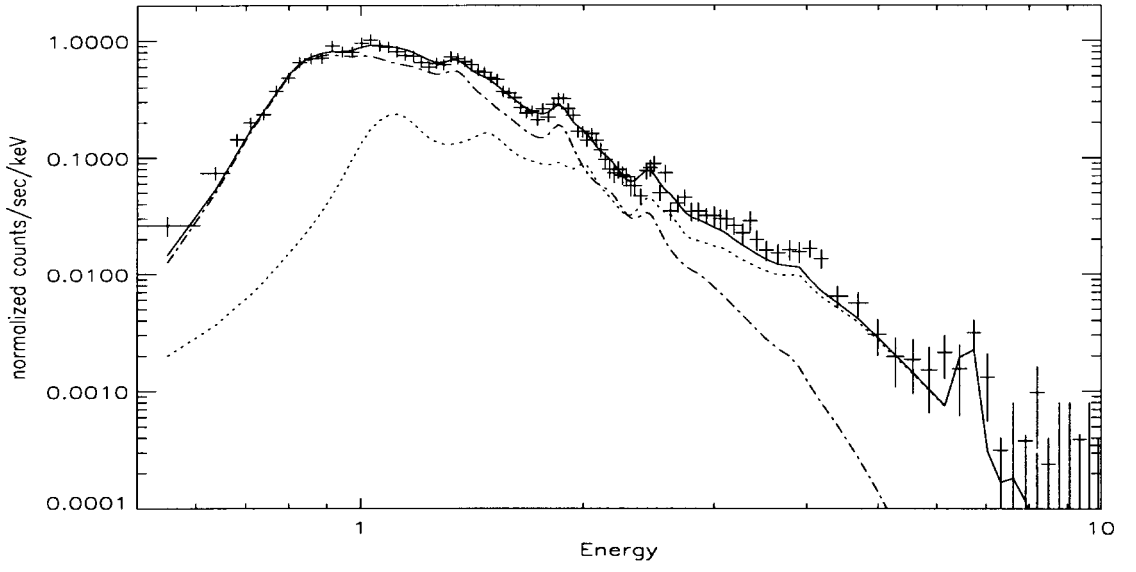

Fig. 10d

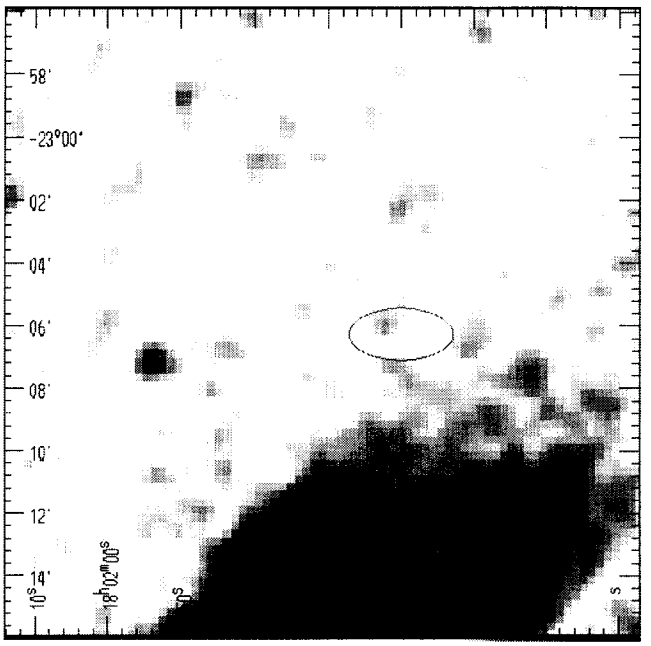

Fig. 11